

Article

# Comparative Study on the Cavitation Erosion and Sliding Wear of Cold-Sprayed Al/Al<sub>2</sub>O<sub>3</sub> and Cu/Al<sub>2</sub>O<sub>3</sub> Coatings, and Stainless Steel, Aluminium Alloy, Copper and Brass

Mirosław Szala <sup>1,\*</sup>, Leszek Łatka <sup>2,\*</sup>, Mariusz Walczak <sup>1</sup> and Marcin Winnicki <sup>2</sup>

<sup>1</sup> Department of Materials Engineering, Faculty of Mechanical Engineering, Lublin University of Technology, Nadbystrzycka 36D, 20-618 Lublin, Poland; m.walczak@pollub.pl

<sup>2</sup> Faculty of Mechanical Engineering, Wrocław University of Science and Technology, 5 Łukasiewicza Street, 50-371 Wrocław, Poland; marcin.winnicki@pwr.edu.pl

\* Correspondence: m.szala@pollub.pl (M.S.); leszek.latka@pwr.edu.pl (L.Ł.)

Received: 30 May 2020; Accepted: 22 June 2020; Published: 28 June 2020



**Abstract:** The paper investigates the cavitation erosion (CE) and sliding wear (SW) resistance of cold-sprayed Al/Al<sub>2</sub>O<sub>3</sub> and Cu/Al<sub>2</sub>O<sub>3</sub> composites and studies them in relation to a set of metallic materials such as aluminium alloy (AlCu4Mg1), pure copper (Cu110), brass (CuZn40Pb2) and stainless steel (AISI 304). The coatings were deposited on stainless steel by low-pressure cold spray (LPCS) using Al (40 wt.%) and Cu (50 wt.%) blended with Al<sub>2</sub>O<sub>3</sub> (60 and 50 wt.%, respectively) feedstocks. CE resistance was estimated by the stationary sample method according to the ASTM G32 standard. The SW test was conducted using a ball-on-disc tester with compliance to the ASTM G99 standard. Results obtained for the LPCS coatings show that the Cu/Al<sub>2</sub>O<sub>3</sub> coating exhibits a denser structure but lower adhesion and microhardness than Al/Al<sub>2</sub>O<sub>3</sub>. The Al/Al<sub>2</sub>O<sub>3</sub> and Cu/Al<sub>2</sub>O<sub>3</sub> resistance to cavitation is lower than for bulk alloys; however, composites present higher sliding wear resistance to that of AlCu4Mg1, CuZn40Pb2 and stainless steel. The CE wear mechanisms of LPCS composites start at the structural discontinuities and non-uniformities. The cavitation erosion degradation mechanism of Al/Al<sub>2</sub>O<sub>3</sub> relies on chunk material detachment while that of Cu/Al<sub>2</sub>O<sub>3</sub> initiates by alumina removal and continues as layer-like Cu-metallic material removal. CE damage of metal alloys relies on the fatigue-induced removal of deformed material. The SW mechanism of bulk alloys has a dominant adhesive mode. The addition of Al<sub>2</sub>O<sub>3</sub> successfully reduces the material loss of LPCS composites but increases the friction coefficient. Coatings' wear mechanism has an adhesive-abrasive mode. In both CE and SW environment, the behaviour of the cold-sprayed Cu/Al<sub>2</sub>O<sub>3</sub> composite is much more promising than that of the Al/Al<sub>2</sub>O<sub>3</sub>.

**Keywords:** cavitation erosion; sliding; wear; friction coefficient; failure mechanism; cold spray; composite; copper; aluminium; alumina; MMC

## 1. Introduction

Abrasion, erosion and sliding cause failure in various applications, e.g., in oil and gas, offshore or mining industries. Abrasion and erosion appear due to wear by abrasive particles or by the impact and entrainment of hard-faced particles in a transport fluid. Sliding wear (SW) is an effect of motion of two moving bodies with different relative velocity magnitudes and/or directions. Moreover, the liquid itself can induce material degradation in the form of liquid impingement erosion, cavitation erosion (CE) or corrosion [1–4]. Metallic materials used in the marine, power and food environments are susceptible to corrosion, erosion or CE damage [5–8]. In most engineering applications abrasion, i.e., sliding wear

(SW), is a dominant type of deterioration. What is more, the appearance of solid wear debris in liquid or gas leads to complex wear processes significantly limiting the service life of metallic components and structures. While deterioration cannot be eliminated entirely, protective coatings can be applied to regenerate and secure the surface of metal parts operated in a harsh environment.

Thermal spraying technologies are widely used to deposit wear-resistant coatings with various materials, the most popular being: High-velocity oxygen fuel (HVOF), plasma spraying or increasingly popular cold spraying. The HVOF spraying technique is widely used in many industries to prevent wear and erosion of components with metal matrix composites (MMCs), e.g., WC-Co [9,10], WC-10Co-4Cr [11], WC-Co/NiCrAlYSi [12], WC-Co-Cr synergized with Mo<sub>2</sub>C/Y<sub>2</sub>O<sub>3</sub>/ZrO<sub>2</sub> [13] or complex alloys FeCrMnCoSi [14,15]. Plasma spraying predominantly includes ceramic coatings, e.g., Al<sub>2</sub>O<sub>3</sub>/TiO<sub>2</sub> [16], Al<sub>2</sub>O<sub>3</sub>/Y<sub>3</sub>Al<sub>5</sub>O<sub>12</sub> [17], TiB<sub>2</sub> [18], complex alloys, e.g., NiCrBSi [19], NiCrMoY [20], CoMoCrSi [21] as well as TiO<sub>2</sub>-NiAl composites [22]. However, additional remelting by laser or vacuum treatment is necessary to decrease the coating porosity or modify its composition by precipitates of hard phases. What is more, both spraying processes may considerably change the chemical composition of original powders by undesired compounds and interlamellar oxidation as well as negatively affect the substrate properties. These defects may be detrimental to corrosion resistance, strength and machinability [23,24], and thus make the fabrication process for coatings more complex and costly.

Cold spray (CS) is a solid-state material deposition method with the feedstock heated to a temperature well below the melting point [25]. There are two main techniques of cold spraying: (i) Low-pressure cold spray (LPCS) and (ii) high-pressure cold spray (HPCS). The general difference between the two is the pressure value which is up to 1 MPa and 5 MPa for LPCS and HPCS, respectively. Moreover, the temperature of the working gases is higher in the HPCS method. These two factors result in a considerable improvement of deposition efficiency in the HPCS process. Besides, the cost of HPCS is significantly higher than that of LPCS [26]. Therefore, CS is used for thin/thick coating deposition, metal surface repair, wear and corrosion prevention and additive manufacturing, which has attracted much attention in aerospace, marine and offshore, oil and gas, power and automotive industries [27,28]. The coating is formed due to extensive plastic deformation of particles upon impact owing to a high velocity. Therefore, the micro-sized particles have to be accelerated in a supersonic gas flow above the critical velocity to achieve bonding between the sprayed material and substrate [25,29]. As successful bonding is attributed to the occurrence of adiabatic shear instability, a local metallurgical bond can occur together with mechanical interlocking. CS is a process with a low working temperature, and thus it poses problems associated with high-temperature processing of materials, such as oxidation, distortion, residual stress and/or harmful microstructural changes [30,31]. Consequently, this method is more suitable for the deposition of temperature-sensitive materials (e.g., Al, Mg) than the conventional thermal spray process. Moreover, the performance of cold-sprayed coating can be improved by applying reinforcement to the feedstock, e.g., ceramic or hard metal powders [32,33]. The reinforcing phase increases plastic deformation of the base metal particles via the tamping effect by eliminating the coating's porosity [25,34] and at the same time increasing the coating properties such as hardness [35,36], wear resistance [36,37] and corrosion resistance [34,38].

Studies on the application of the CS method to produce metallic materials or MMCs reinforced with ceramic particles are systematically reported in literature. Generally, the production of aluminium [28,39], copper [5,36] and other metallic cold-sprayed coatings is still investigated with respect to improving the microstructural and functional properties of final deposits. Nowadays researchers investigate different composite systems such as Mg/SiC [40], Al/SiCp/Al5056 [41], Al/Al<sub>2</sub>O<sub>3</sub> [42,43], Ni/Al-TiB<sub>2</sub> [44], Ni/Al<sub>2</sub>O<sub>3</sub> [45], Inconel718-Ni [7], Zn-Al [46], Zn-Al-Mg-TiO<sub>2</sub> [47], Cu/Al<sub>2</sub>O<sub>3</sub> [36], Cu/SiC [34], different matrixes (Al, Cu, Zn, Sn and Ni) reinforced with Al<sub>2</sub>O<sub>3</sub> [48] or a nickel-based matrix with WC, TiC, B<sub>4</sub>C particles [35]. According to Sova et al. [49], the fine ceramic particles significantly affect the deposition efficiency of the metal-ceramic powder mixture and promote adhesion by roughening the previously deposited coating surface. WC is a popular ceramic in MMCs due to its excellent resistance to sliding, abrasive and erosive wear [50]. More and more popular are chemically

stable and highly corrosion-resistant titanium carbide (TiC) and boron carbide (B<sub>4</sub>C) with higher hardness values than that of WC [35]. The most popular ceramic powders used as a reinforcing phase in cold spraying are SiC and Al<sub>2</sub>O<sub>3</sub>. However, since Al<sub>2</sub>O<sub>3</sub> exhibits a higher corrosion resistance and chemical stability than SiC, it is more widely used in the anticorrosion technology [51].

CS aluminium and copper coatings have been successfully deposited on various substrates metallic substrates. Extensive studies have been recently performed on coating formation, process simulation and properties, as well as bond strength, abrasion wear resistance, corrosion resistance and electrical conductivity. While pure aluminium or copper cold-sprayed coatings have high corrosion resistance and electrical conductivity, they exhibit poor wear resistance [43]. On the one hand, ceramic powder admixtures provide additional phases in the coating, enabling corrosion penetration [34]. On the other, they densify the composite microstructure, hence minimizing the presence of porosity and thus increasing the coating's properties [43]. Irissou et al. [52] studied the properties of Al-Al<sub>2</sub>O<sub>3</sub> coatings deposited by CS and found that the MMC coatings were as effective as pure-Al coatings in providing corrosion protection. Winnicki et al. [34] demonstrated that relatively high porosity of a pure metallic Cu coating contributed to its lower corrosion resistance. Moreover, lower porosity of MMC coatings in comparison to the metallic Cu coating resulted in a higher electrical conductivity. Meydanoglu et al. [53] concluded that the addition of ceramic particles to 7075 Al powder improved the wear performance of the cold-sprayed coatings significantly. Among the composite coatings, B<sub>4</sub>C-reinforced composite coatings exhibited higher wear resistance when compared to SiC, which was attributed to the elastic modulus and particle size differences [53].

A literature survey confirms that the wear prevention of cold-sprayed deposits constitutes an emerging and up-to-date problem. The application of cold-sprayed coatings is still developed and their anti-wear or anti-erosion properties are investigated. While the literature of the subject reports many studies describing the SW mechanism of cold-sprayed Al- [36,43,54] and Cu-based [31,38,54] composites, there are no studies devoted to the cavitation erosion resistance (CER) of such materials. According to the literature, the CER of cold-sprayed materials has been studied for a limited range of deposits, namely Ni/Al<sub>2</sub>O<sub>3</sub> [45], nickel-Inconel 718 composite coatings [55], Cu-Al-bronzes [5]. Moreover, due to the fact that there is no information about the CE behaviour of Al/Al<sub>2</sub>O<sub>3</sub> and Cu/Al<sub>2</sub>O<sub>3</sub> composites, the present is the first study to describe the CER and wear mechanism of these materials.

Most studies investigate the SW and CE of coatings separately, and few works provide a comprehensive description of their wear behaviour [56–58]. What is more, sliding test conditions (e.g., applied load, velocity or sliding distance) affect obtained results. Even though the SW of LPCS deposited Al- and Cu-based composites have been reported, the literature of the subject does not describe the SW mechanisms of Al/Al<sub>2</sub>O<sub>3</sub> and Cu/Al<sub>2</sub>O<sub>3</sub> coatings under similar test conditions. Additionally, there is no study on the CE mechanism in both Al- and Cu-based MMCs. Therefore, this paper investigates the SW and CE behaviour of cold spray-deposited Al/Al<sub>2</sub>O<sub>3</sub> and Cu/Al<sub>2</sub>O<sub>3</sub> coatings.

It should be emphasized that the limited available publications discuss the CE and SW performance of Al/Al<sub>2</sub>O<sub>3</sub> and Cu/Al<sub>2</sub>O<sub>3</sub> coatings with popular metal alloys. This work, in turn, compares a wide range of commercial alloys, such as alumina alloy (AlCu4), pure copper (Cu110), brass (CuZn40) and stainless steel (SS 304), in relation to low-pressure cold-sprayed MMC coatings. This work combines information about the functional properties of LPCS composite coatings and metal alloys. Thus, results obtained in this study can be useful for future applications of the CS technology in the industry, and reconsider its sliding and cavitation wear performance LPCS composites.

This study describes the cavitation erosion (CE) and sliding wear (SW) behaviour of low-pressure cold-sprayed Al/Al<sub>2</sub>O<sub>3</sub> and Cu/Al<sub>2</sub>O<sub>3</sub> coatings. In addition, the work discusses the CE and SW mechanisms of LPCS deposited composites and compares it with commercial Al- and Cu-based metallic materials.

## 2. Materials and Methods

### 2.1. Fabrication of Cold-Sprayed Coatings and Material Codes

The starting powders were commercially available metallic feedstock materials, namely—aluminium (K-10-01, purity: 99.6%), electrolytic copper (K-01-01, purity: 99.5%) and alumina ( $\text{Al}_2\text{O}_3$ , purity: 99.6%) powders (manuf. Obninsk Center for Powder Spraying, Obninsk, Russia). The feedstock powders have the following morphology: Aluminium—spherical, copper—dendritic and  $\text{Al}_2\text{O}_3$ —crushed. For deposition of the  $\text{Al}/\text{Al}_2\text{O}_3$  and  $\text{Cu}/\text{Al}_2\text{O}_3$  composites, the powders were blended Al (40 wt.%) +  $\text{Al}_2\text{O}_3$  (60 wt.%) and Cu (50 wt.%) +  $\text{Al}_2\text{O}_3$  (50 wt.%), respectively. Granulometry tests (Analysette 22 MicroTec plus, Fritsch, Markt Einersheim, Germany) revealed that the metallic powder particle size was in the range  $-50 + 10 \mu\text{m}$ , while for the ceramic powder it was  $-30 + 20 \mu\text{m}$ . The main  $d_{vs}$  (volume to the surface) diameter of the prepared  $\text{Al}/\text{Al}_2\text{O}_3$  and  $\text{Cu}/\text{Al}_2\text{O}_3$  feedstock powders was  $23.7 \mu\text{m}$  and  $24.5 \mu\text{m}$ , respectively. Figure 1 presents the morphology of the feedstock powders. Stainless steel substrates (AISI 304) were disc-shaped with 25 mm in diameter and 2 mm in thickness. Before LPCS deposition, the substrate was finished by grinding, roughness yielding a  $R_a$  of  $0.4\text{--}0.6 \mu\text{m}$  (Surtronic S-128, Taylor-Hobson, Leicester, UK) and cleaned with ethanol. Feedstock powder was deposited on an AISI 304 substrate by low-pressure cold spray (LPCS) to obtain a coating of  $0.75\text{--}1.0 \text{ mm}$  in thickness. The  $\text{Al}/\text{Al}_2\text{O}_3$  and  $\text{Cu}/\text{Al}_2\text{O}_3$  composites were manufactured using a Dymet 413 gun (Obninsk Center for Powder Spraying, Obninsk, Russia) provided with a de Laval nozzle. The nozzle had the throat diameter of 2.5 mm and the inner exit diameter of 5 mm. The gun was mounted on the arm of a 3-axis BZT PF 600-P manipulator (Sorotec GmbH, Rheinmünster, Germany). Air was used as a working gas, and the distance between the next gun passes was set equal to 2 mm. Detailed process parameters are given in Table 1.

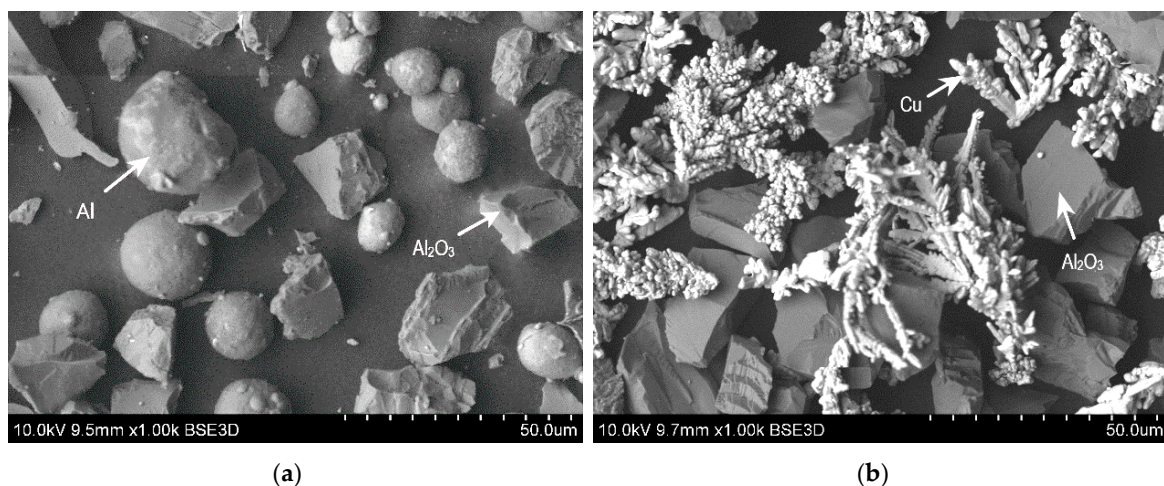


**Figure 1.** Feedstock powders used for metal matrix composite (MMC) coating deposition: (a)  $\text{Al}/\text{Al}_2\text{O}_3$  (b)  $\text{Cu}/\text{Al}_2\text{O}_3$ .

**Table 1.** Spray parameters of low-pressure cold-sprayed composite coatings.

Sample Code	Gas Temperature	Gas Pressure	Spray Distance	Gun Travel Speed	Powder Feeding Rate
$\text{Al}/\text{Al}_2\text{O}_3$	473 K	0.9 MPa	10 mm	10 mm/s	30 g/min
$\text{Cu}/\text{Al}_2\text{O}_3$	873 K				

To compare the wear behaviour of the Al- and Cu-based metal matrix composites (MMCs), a set of commercial metallic materials: Aluminium alloy, pure copper, brass and stainless steel was selected. The 30 mm diameter rods were cut and machined by turning, to obtain a cylinder-shaped test samples with a minimal height of 5 mm. Prior to cavitation and sliding wear testing, the specimen flat

surfaces were finished by grinding with emery papers to achieve the surface roughness of  $R_a < 0.1 \mu\text{m}$  and  $R_z < 1.0 \mu\text{m}$ . Table 2 gives the detailed characteristics of the cold-sprayed MMC coatings and reference materials.

**Table 2.** Investigated materials: Grade, chemical composition and sample codes.

Sample Code	Grade	Nominal Chemical Composition, wt. %		
		Al	Cu	Dominant Component/Element
Al/Al <sub>2</sub> O <sub>3</sub>	Composite coated AISI 304	40	-	Alumina (Al <sub>2</sub> O <sub>3</sub> ) 60%
Cu/Al <sub>2</sub> O <sub>3</sub>	substrate	-	50	Alumina (Al <sub>2</sub> O <sub>3</sub> ) 50%
AlCu4	AlCu4Mg1	~96	4	Mg 1.2–1.8; Mn 0.3–0.9; other
Cu110	Cu-ETP	-	~99.95	O < 0.05
CuZn40	CuZn40Pb2	-	~60	Zn 40; Pb < 2; Fe < 0.7
SS304	AISI 304	-	-	Fe bal.; Cr 18; Ni 10; C < 0.05, other

## 2.2. Characterization Methods

Surface morphology and cross-sectional microstructure of cold-sprayed coatings were examined with the use of a profiler (Surtronic S-128, Taylor-Hobson, Leicester, UK) and scanning electron microscope equipped with an energy dispersive spectrometer (SEM-EDS, Phenom ProX Desktop SEM, Phenom World (Waltham, MA, USA)).

Vickers HV0.1 hardness (load 100 g, dwelling time 10 s) of the composites and reference metallic samples was measured on the flat surfaces (finished by grinding with emery paper grit 600), and at least 10 indentations were made to ensure statistical accuracy. Additionally, hardness HV0.1 of the coatings was measured on the as-sprayed cross-section in three specified areas: Near the coating top surface; in the middle of the transverse of the coating; and in the vicinity of the coating-substrate interface.

The coating's adhesion to the substrate was estimated in compliance with a tensile pull-off test described in the ISO 14916:2017-05 standard, its procedure details having been given in previous papers [42,48,59]. Three tests were carried out for each experimental run and the average adhesion value was determined. The adhesion value was determined as the ratio of the maximum load to the cross-sectional area of the sample.

## 2.3. Wear Test Conditions

Wear test results of the MMCs were discussed in relation to the reference materials, i.e., aluminium alloy, pure copper, brass and stainless steel, described in Table 2. Prior to sliding and cavitation wear testing, the metal alloy surfaces were finished by grinding. Additionally, the cavitation test was performed for both ground and as-sprayed (without surface machining) coating surface finish.

Cavitation erosion tests were prepared using a vibratory test rig and test conditions described in previous papers [58,60]. Cavitation was generated by a magnetostrictive-driven apparatus Sonics VCX500 (Sonics & Materials Inc., Newtown, CT, USA), resonating at 20 kHz with a peak-to-peak displacement amplitude of 50  $\mu\text{m}$ . The standoff between the sonotrode-tip and the specimen surface was set equal to 1–0.05 mm. The apparatus conformed to the ASTM G-32 [61] standard recommendations, and measurements were performed by the stationary specimen method. During the test, at stated time intervals, the samples were examined by precise weighing with a 0.01 mg accuracy analytical balance. The mean depth of erosion (MDE), erosion rate and maximum erosion rate (MER) and incubation period ( $t_0$ ) were determined according to ASTM G-32 [61]. After that, erosion stages were read from the plotted cumulative cavitation curves. To identify the wear mechanism, the worn surfaces were tested with a surface profilometer and examined by SEM-EDS using BSE and topographic modes.

Tribological behaviours of the composite coatings and reference metal alloys were investigated in dry sliding conditions at room temperature using a CSM Instruments tribometer (CSM Instruments SA, Peseux, The Switzerland). Measurements were performed by the ball-on-disc method according to the ASTM G99 standard [62]. The WC-Co counterpart ball diameter was set equal to 6 mm. The applied load, sliding speed and sliding distance were 10 N, 100 mm/s and 200 m, respectively. During each

test, the coefficient of friction (COF) was plotted versus sliding distance. In order to investigate wear behaviour, wear track morphology was examined by scanning electron microscopy (SEM) in combination with EDS and topo-mode. Moreover, worn surfaces were analysed with a surface profiler (Dektak 150, Veeco Instruments Inc., Plainview, NY, USA), and the wear factor ( $K$ ) was estimated in compliance with the Equation (1) [63]. The SW mechanism as well as the wear factor and COF of the cold-sprayed composites were analysed in relation to the reference metal alloys described in Table 2.

$$K = \frac{\text{Wear volume}}{\text{Applied force} \cdot \text{Sliding distance}}, \text{ mm}^3\text{N}^{-1}\text{m}^{-1} \quad (1)$$

### 3. Results and Discussion

#### 3.1. Composite Microstructure and Properties

Figure 2 shows the as-sprayed and machined-by-grinding surfaces of the Al/Al<sub>2</sub>O<sub>3</sub> and Cu/Al<sub>2</sub>O<sub>3</sub> coatings, while their cross-sections are shown in Figure 3. The rough top surfaces of the as-deposited coatings are characterized by wavy morphology corresponding to passes of the cold spray gun, which is typical of the CS technology [64]. According to Yu and Li [65], the “soft” metal matrix with extensive plastic deformation adheres to the substrate surface as well as to the previously deposited layers. The hard particles of alumina onlypeen the layers and mechanically wedge in the deposited matrix or are embedded by the incoming “soft” matrix. The dual MMC microstructure consists of the ceramic particle Al<sub>2</sub>O<sub>3</sub> bonded by the metallic Al- or Cu-matrix. According to Chen [36], when spraying the blends of Cu/Al<sub>2</sub>O<sub>3</sub>, the addition of alumina can result in a mechanical hammering effect of the alumina particles, which is promising for the elimination of pure copper porosity. Apart from the dense solid copper matrix visible in Cu/Al<sub>2</sub>O<sub>3</sub>, the presence of pores and Al<sub>2</sub>O<sub>3</sub> particles stacked in the metallic matrix is confirmed in Al/Al<sub>2</sub>O<sub>3</sub> (Figures 2 and 3). Besides, no aluminium oxidation is observed, which—according to the previous paper [42]—can be explained by the CS technological parameters that prevent the metallic particles from oxidation. Moreover, during spraying the ceramics undergo fragmentation and form fine alumina particles that are agglomerated in the Al matrix. As a result, micropores are created in the ceramic clusters and at the ceramic-metallic interfaces as a result of low adhesion of the fragmented Al<sub>2</sub>O<sub>3</sub>-ceramic particles to the Al-metallic matrix. On the other hand, in the case of Cu/Al<sub>2</sub>O<sub>3</sub>, the Al<sub>2</sub>O<sub>3</sub> particles distribute randomly in the copper matrix. Apart from that, the cross-section microstructure, shown in Figure 3, indicates no visible delamination at the coating-substrate interface, which suggests that the coatings adhere well to the substrate. The interface between the coatings and the substrate shows no cracks, porosity or other discontinuities. This observation is supported by the adhesion pull-off test results given in Figure 4. The adhesion of the Al and Cu coatings to the stainless steel substrate is 41.6 MPa and 33.9 MPa, respectively. Summing up, the adhesion of cold-sprayed composites is relatively high. Consequently, it exceeds the adhesion of coatings deposited by other thermal spray techniques, which is: 21.3 MPa for commercially pure Al [66] and 13.7–16.3 MPa for Al<sub>2</sub>O<sub>3</sub>-10% TiO<sub>2</sub> [59] coatings deposited by atmospheric plasma spraying (APS) or 12.8 MPa for Al reinforced with SiC fabricated by HVOF [67]. Moreover, the adhesion reported for Al/Al<sub>2</sub>O<sub>3</sub> was approx. 10 MPa lower while that obtained for Cu/Al<sub>2</sub>O<sub>3</sub> exceeded twofold the results obtained in our earlier works [42,48]. These differences can be explained by the use of different fabrication parameters in the present study. Specifically, in this work, we applied a lower LPCS spray temperature and used an AISI 304 substrate type with ground surface finish.

A comparison of Vickers hardness of the composites and reference metal alloys is given in Figure 5a, while the results of hardness analysed in the coatings transverse is given in Figure 5b. The hardness of the LPCS composites is similar to that of Al- and Cu-based alloys. The obtained Vickers hardness agrees with the results reported in the literature for metal alloys [68,69] and cold-sprayed coatings [36,42,48,54] (sprayed with different CS process parameters). Therefore, the composites have a lower mean hardness than metal alloys and are softer than brass and stainless steel. The average Cu/Al<sub>2</sub>O<sub>3</sub> hardness is similar to that of pure copper while the average hardness of Al/Al<sub>2</sub>O<sub>3</sub> is in a

range for an Al-rich AlCu4 sample. This indicates a dense structure of the cold-sprayed materials. The difference in the cross-sectional hardness results confirms the two-phase structure and indicates a uniform range of hardness along with a coating depth. The coatings have an excellent adhesion to the substrate and their hardness is on a comparable level to that of their bulk alloy equivalents, which will guarantee good machinability of the LPCS composites. This will facilitate surface finishing of coatings for future engineering applications.

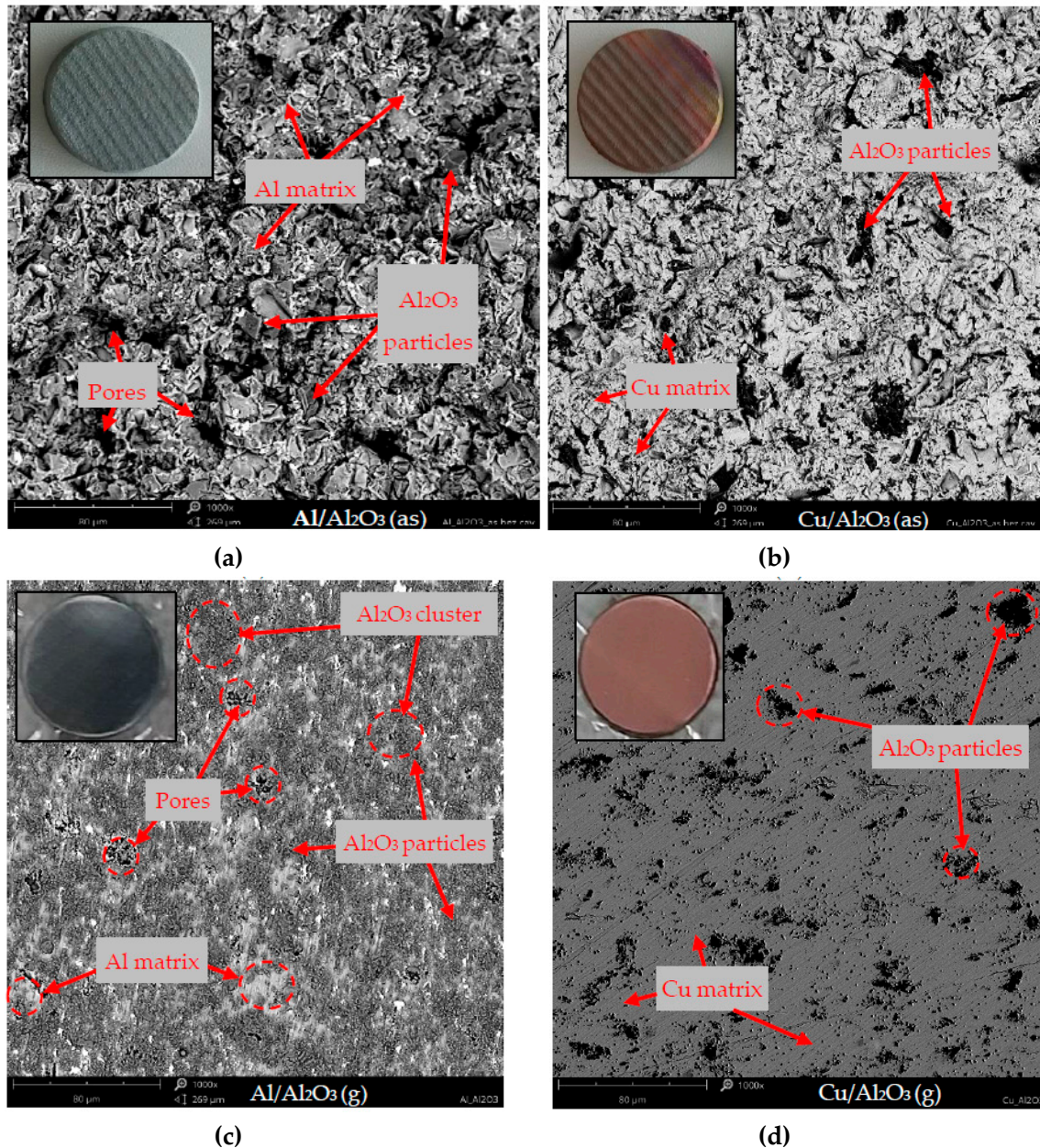


**Figure 2.** Surface morphology of composites: (a) As-sprayed Al/Al<sub>2</sub>O<sub>3</sub>; (b) as-sprayed Cu/Al<sub>2</sub>O<sub>3</sub>; (c) ground Al/Al<sub>2</sub>O<sub>3</sub> and (d) ground Cu/Al<sub>2</sub>O<sub>3</sub>, macrophoto and SEM-BSE.

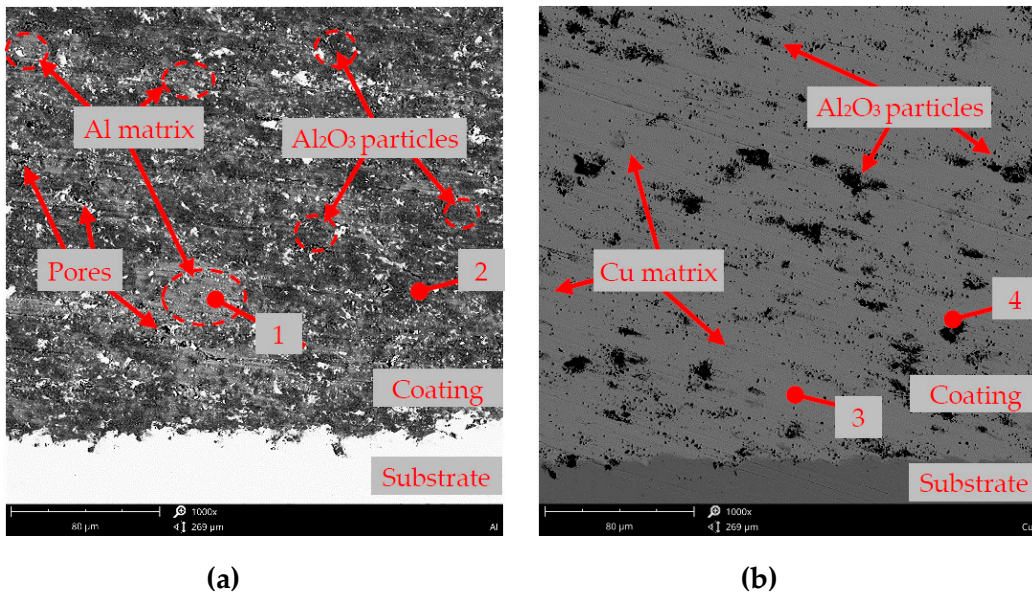


**Figure 3.** Cross-sectional microstructure of cold-sprayed MMCs on AISI 304 substrate: (a) Al/Al<sub>2</sub>O<sub>3</sub> (b) Cu/Al<sub>2</sub>O<sub>3</sub>. SEM-EDS chemical analysis in spots: 1—Al 94.7%, O 5.3%; 2—Al 56.4%, O 43.6%; 3—Cu 100%, 4—Al 66.6%, O 33.4%; (wt.%).

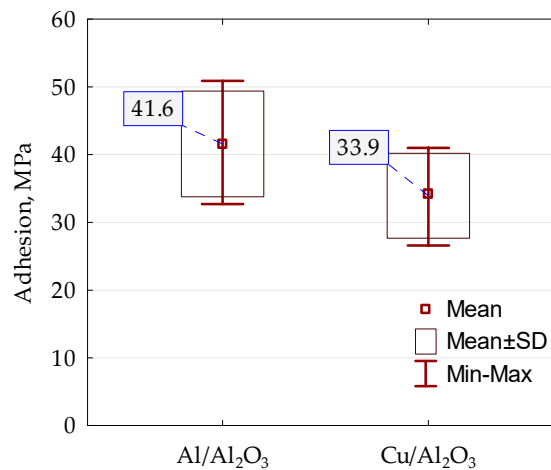


**Figure 4.** Adhesion of MMC coatings.

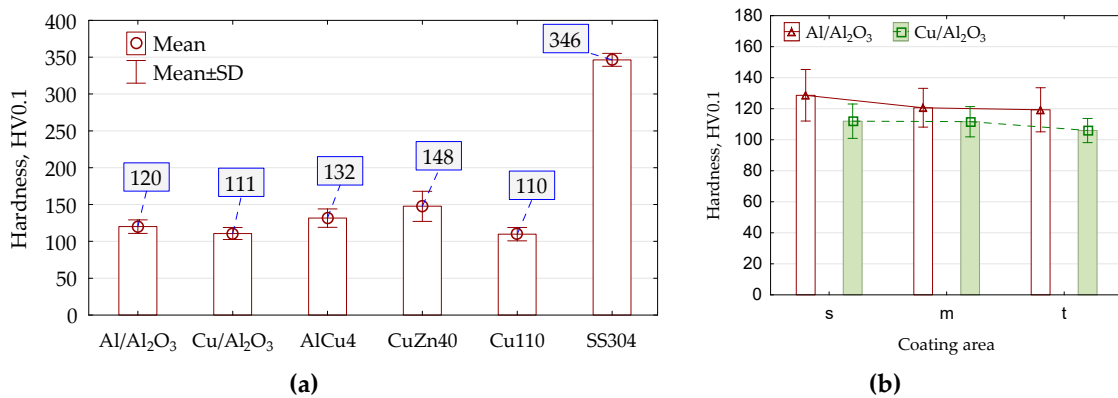


**Figure 5.** Hardness results: (a) Hardness of metal alloys and MMCs measured on their surface (b) hardness of MMCs estimated in their cross-sections: In the area located near the coating-substrate interface (s), in the middle of the coating thickness (m) and in the vicinity of the coating top (t).

### 3.2. Cavitation Erosion (CE) of Coatings and Bulk Alloys

The surfaces of as-sprayed and machined MMCs as well as of the reference bulk alloys were examined for CER. An overview of the damaged surfaces and profiles with estimated volume loss is shown in Figure 6. The centre of the sample is a cavitation-damaged area, while the outer region is the initial sample surface that was not affected by cavitation. A comparison of the eroded areas allows us to state that metal alloys exhibit a less rough surface and a smaller erosion depth than composites. The as-sprayed coatings have developed wear with a considerable surface material detachment. The progress of erosion behaviour is described in detail quantitatively—Figure 7 shows the plots comparing the cumulative erosion of the specimens, while Table 3 gives the estimated MER and incubation time  $t_0$ . A complex analysis of the CE results reveals that the Cu/Al<sub>2</sub>O<sub>3</sub> composite coatings have a higher CER than the Al/Al<sub>2</sub>O<sub>3</sub> composite. However, both cold-sprayed coatings show a lower resistance to cavitation than the reference bulk alloys. Additionally, the aluminium-based materials (Al/Al<sub>2</sub>O<sub>3</sub>, AlCu4) have a higher wear rate than the copper-based materials (Cu/Al<sub>2</sub>O<sub>3</sub>, Cu110 and CuZn40) or stainless steel (SS304). This observation is in agreement with the literature findings regarding the CER of light metal alloys [70,71] and brass [72,73].

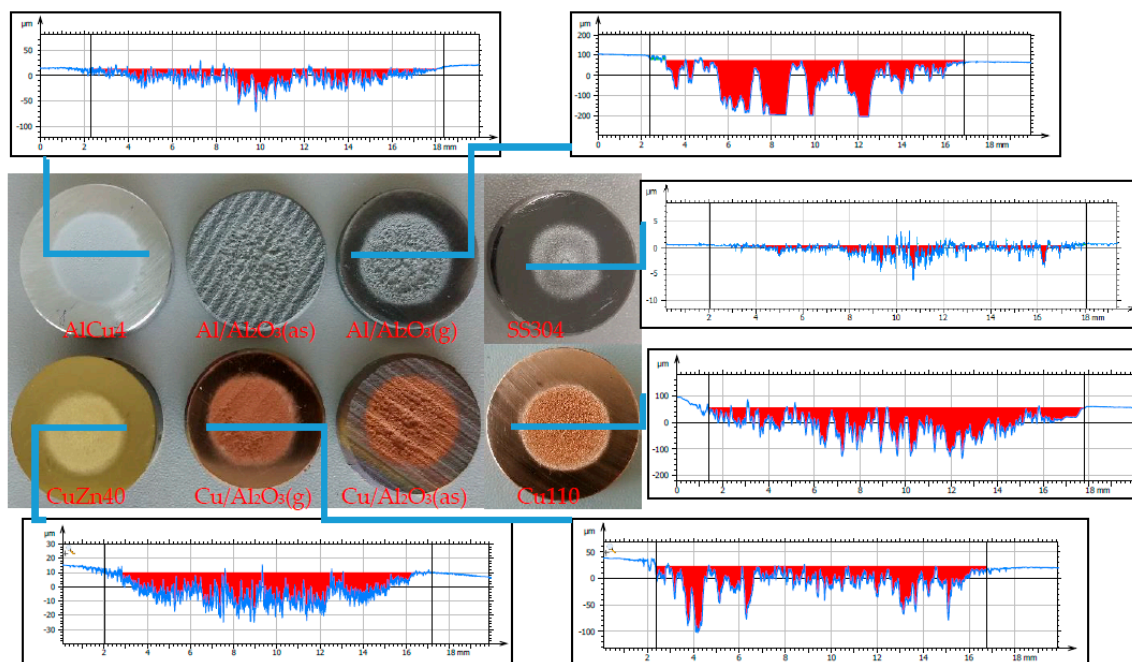


**Figure 6.** Comparison of the eroded surfaces and cross-sectional profiles of ground samples (different range of depth of the Y-axis in the profilograms), 30 min of cavitation erosion testing; as-sprayed (as) and ground (g).

**Table 3.** Cavitation erosion indicators of tested MMC coatings and metal alloys.

Cavitation Erosion Parameter	Specimen							
	Al/Al <sub>2</sub> O <sub>3</sub> (as)	Cu/Al <sub>2</sub> O <sub>3</sub> (as)	Al/Al <sub>2</sub> O <sub>3</sub> (g)	Cu/Al <sub>2</sub> O <sub>3</sub> (g)	AlCu4	Cu110	CuZn40	SS304
MER, mm <sup>3</sup> /h	98.2	33.4	69.1	14.8	4.6	10.9	0.7	0
MDE, µm	53.4	21.0	43.5	9.3	2.9	6.8	0.2	0
$t_0$ , min	0	0	0	2	11	6	15	30 *

Composite surface finishes: (g)—ground, (as)—as-sprayed, \*— $t_0$  of SS304 last longer than 30 min of exposure.

The addition of the ceramic (alumina) particles accelerated the wear loss and limited the incubation time of the cold-sprayed metallic samples. It can easily be noticed that the erosion curves of Cu/Al<sub>2</sub>O<sub>3</sub>(g) and Cu110 have a similar shape, as shown in Figure 7b. The main difference between these materials is the presence of alumina in the cold-sprayed composite Cu/Al<sub>2</sub>O<sub>3</sub> (g). This limits the incubation

time of the composites due to the removal of composite ceramic particles. The incubation period is a characteristic stage of the CE of metal alloys [74]. According to the ASTM G32 standard [61], the incubation period is the initial stage of erosion in time when the erosion rate is zero or negligible. Thus, the incubation time of the ground Cu/Al<sub>2</sub>O<sub>3</sub> and reference metal alloys exceeds the zero value. This confirms that the erosion of the Al/Al<sub>2</sub>O<sub>3</sub> samples and as-sprayed Cu/Al<sub>2</sub>O<sub>3</sub> starts with a cavitation load and results in a high erosion rate after only two minutes of cavitation (which is discussed further as a “surface cleaning effect”), see Table 3.

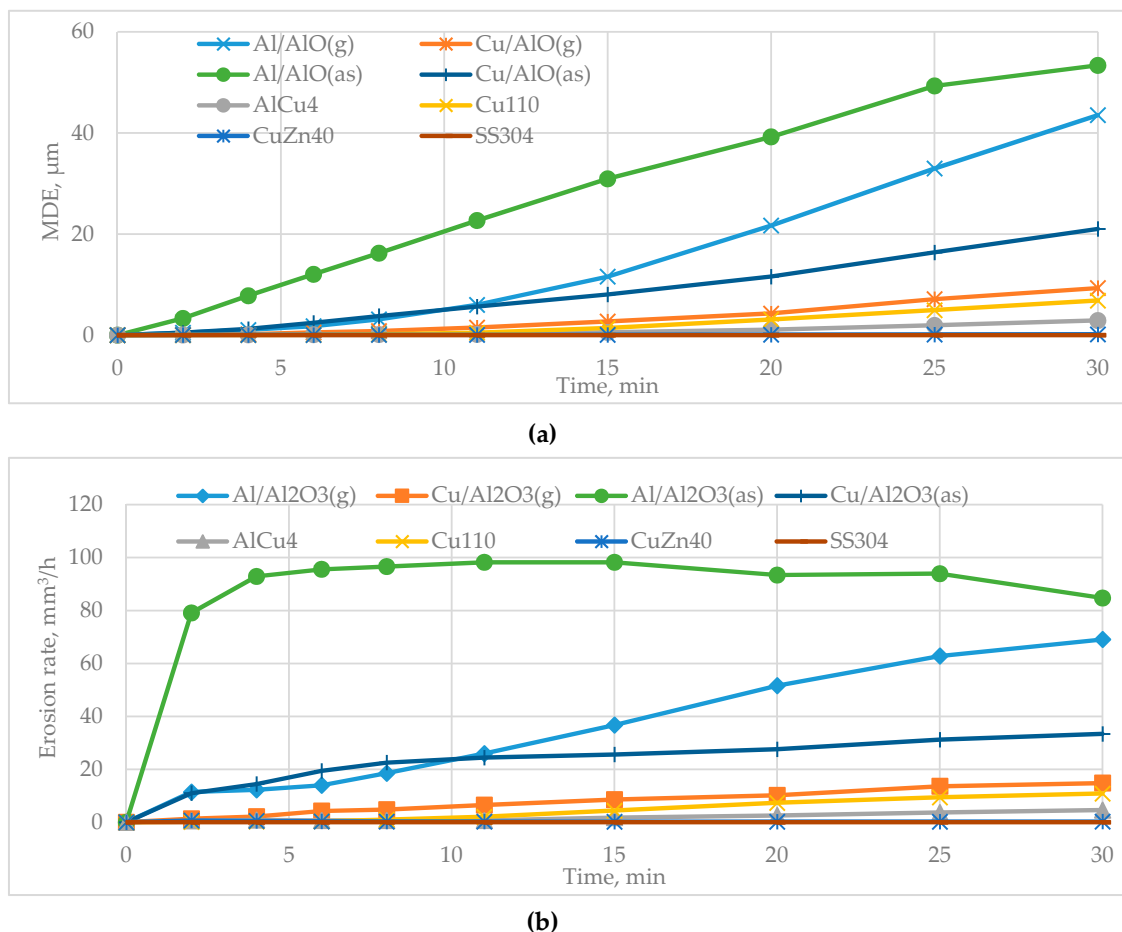


**Figure 7.** Cumulative erosion versus time curves: (a) Mean depth of erosion, MDE; (b) erosion rate. Composites with different surface finish: Ground (g) and as-sprayed (as).

Moreover, the research has confirmed that surface preparation plays a crucial role in the CE behaviour of materials. It can be read in Figure 7 that both as-sprayed coatings exhibit a much more significant material loss than the samples machined by grinding. Moreover, Table 3 indicates an almost twofold increase in the erosion rate of the as-sprayed samples than the ground coatings. This results from high surface roughness, waviness, top surface pores and the presence of poorly adhered sprayed particles on the top of the coatings, see Figure 2. All of the above-mentioned factors accelerate the erosive effect of the materials, which is confirmed by the SEM observations, as shown in Figure 8. A comparison of the undamaged surfaces in Figure 2 with the damaged ones shown in Figure 8 confirms that the general wear mechanism of the coatings starts at structural discontinuities and non-uniformities, ceramic-metal matrix interfaces or pores. The erosion of the as-sprayed composites initiates with a “surface cleaning effect” consisting in the removal of poorly embedded ceramic and metallic particles or starts at rough surface dimples.

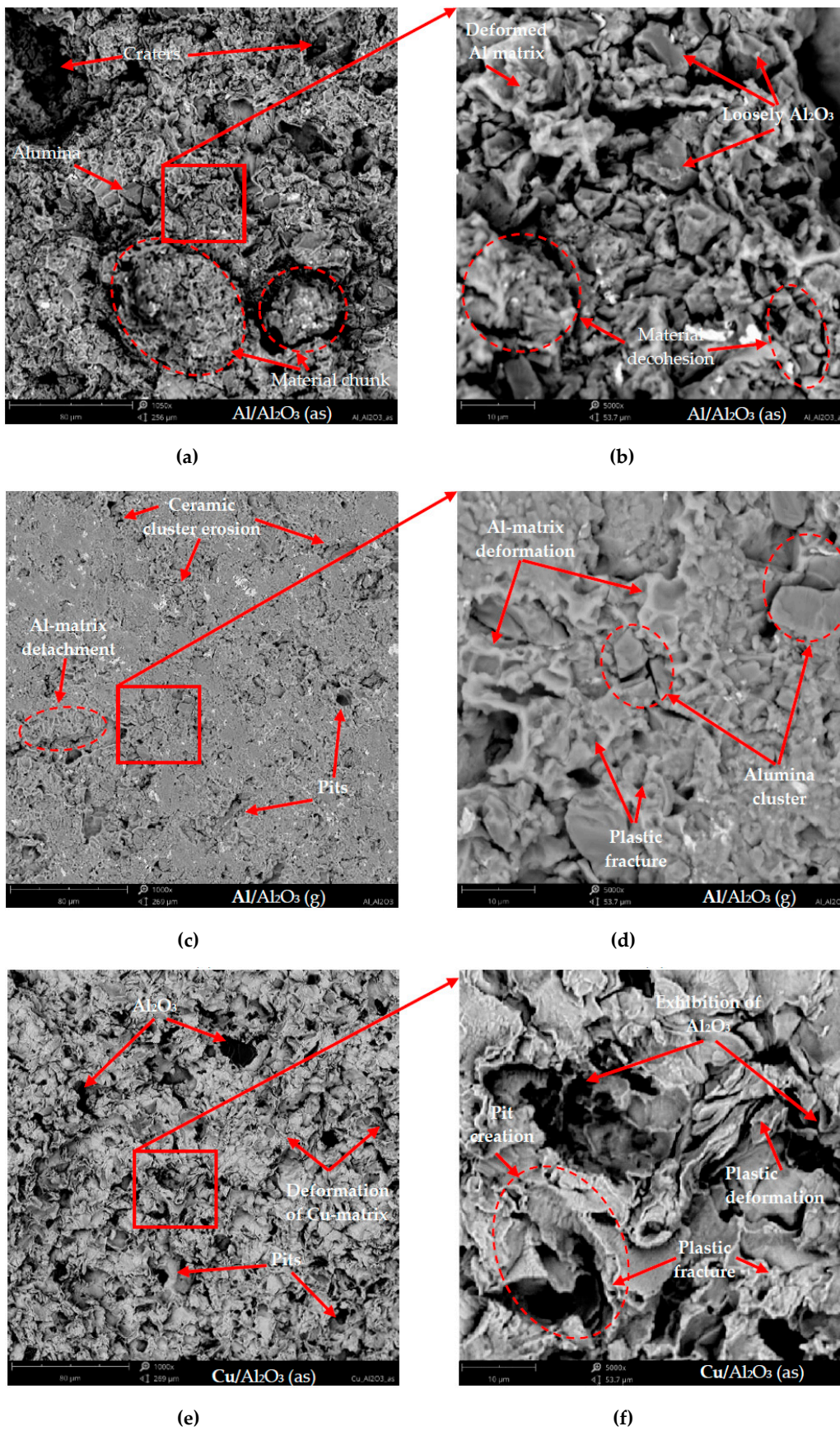
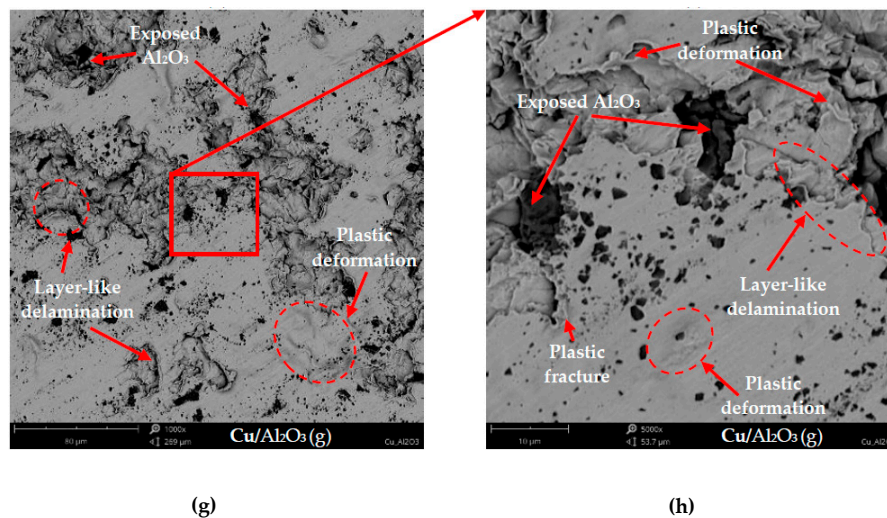


Figure 8. Cont.



**Figure 8.** Cavitation-eroded composite surfaces: As-sprayed (as) and finished by grinding (g) (Figure 2 shows the preliminary surface morphologies): (a–d) Al/Al<sub>2</sub>O<sub>3</sub>; (e–h) Cu/Al<sub>2</sub>O<sub>3</sub> coatings, SEM.

However, the cavitation wear mechanisms of the Al/Al<sub>2</sub>O<sub>3</sub> and Cu/Al<sub>2</sub>O<sub>3</sub> coatings differ due to their microstructural differences. In the case of Al/Al<sub>2</sub>O<sub>3</sub>, the poorly cohered material chunks, alumina clusters and particles are first removed, see Figure 8a–d. Then, the cavitation deforms the Al-matrix, and thus the alumina loses its mechanical interlocking and is detached. The ceramics located in the clusters (compare with Figure 2) are also removed; therefore, at the initial stage of erosion, large pits are formed, as shown in Figure 8c,d. As a result, the coherence of material microstructure is weakened, leading to the detachment of massive chunks of the coating material. This CE wear mechanism was also identified in our previous work [73] for Al<sub>2</sub>O<sub>3</sub>-40%TiO<sub>2</sub>/NiMoAl composites. Once the surface is roughened, the erosion quickly progresses into deeper areas of the composite. Similarly, the erosion of Cu/Al<sub>2</sub>O<sub>3</sub> starts with the removal of ceramics and continues due to the plastic deformation of the Cu-matrix; consequently, pits are formed in the metallic areas, as shown in Figure 8e–h. The damage mechanism consists in the removal of fatigue-deformed copper located in the ceramic particles. Due to the action of cavitation load, the alumina located underneath loses the bonding with the fatigue-deformed metallic matrix, and consequently a layered portion of the Cu-material is detached, see Figure 8h. Then, the exposed alumina erodes and the cavitation damage progresses into deeper regions of the material.

It should be emphasized that the erosion mechanisms of the Al/Al<sub>2</sub>O<sub>3</sub> and Cu/Al<sub>2</sub>O<sub>3</sub> coatings differ in that the Al-coating particles are detached as chunks of material while the Cu-composite material is removed in layers. The cavitation behaviour of materials primarily depends on the type of metal matrix. Copper alloys have a low stacking-fault energy, in contrast to a relatively high stacking-fault energy of aluminium. The work hardening rate in combination with the low stacking-fault energy under high stress and the material's ability to high strain rate deformation induced by cavitation load are responsible for the high CER [75,76]. Moreover, hardness, elastic modulus and fatigue strength are other key factors affecting the anti-cavitation properties of a material [77,78]. Cu alloys have a higher deformability, which consequently leads to their higher cavitation resistance than that of aluminium alloys. This fact agrees well with the quantitative results given in Table 3.

Summing up, the cavitation erosion wear mechanism is affected by MMC microstructure. The damage of Al is intensified by the presence of alumina clusters poorly adhering to the Al-matrix. At the same time, the dense Cu-matrix successfully “absorbs” the cavitation impact and, as a result, undergoes considerable deformation. The deformation leads to fatigue of the Cu-layers located over alumina and, finally, to the detachment of the deformed metallic material.

In contrast, the reference metal alloys exhibit lower erosion rates and prolonged incubation time than the cold-sprayed composites, see Figure 7 and Table 3. Briefly, the reference bulk alloys

have similar CE mechanisms. An analysis of the SEM images of eroded surfaces confirms that the wear behaviour is dominated by plastic deformation, pit formation and subsequent removal of the deformed-material, Figure 9. However, different alloys are characterized by different values of MDE and, consequently, damage intensity. Generally, this can be attributed to material toughness and deformability and usually stems from mechanical properties. First, hard metal alloys are considered resistant to cavitation. Furthermore, the metallic material's phase composition, size and arrangement of microstructural components affect the progression of damage. The same can be observed in our study, as an analysis of the hardness (Figure 5) and CE results of bulk alloys demonstrates that the erosion of soft Cu110 and AlCu4 occurs faster.

In the case of all investigated materials, the surface non-uniformities and discontinuities as well as scratch-edges or microstructure interfaces are the areas where material degradation initiates. In contrast to the Al/Al<sub>2</sub>O<sub>3</sub> and Cu/Al<sub>2</sub>O<sub>3</sub> composites, the mass loss of the reference samples occurring after 4 min is within the range of measurement error; thus, they all are in the incubation stage of CE, see Figure 9 and Table 3. Besides, it can be easily observed when comparing Cu110 (Figure 9a,b) and AlCu4 (Figure 9c,d) that the damage mechanism of both samples relies on plastic deformation and—under higher magnifications—a material pile-up and material loss initiation can be observed, see Figure 9b,d. However, the SEM-EDS examination reveals that the AlCu4 sample has a two-phase microstructure consisting of an  $\alpha$ -Al solid solution and intergranular secondary phases. Hence, after 4 min of testing, the Al-rich solid solution undergoes plastic deformation, as typical of Al-alloys [79], while the intergranular secondary phases undergo erosion rupture. Finally, the  $\alpha$ -matrix undergoes plastic flow that is followed by detachment. In turn, CuZn40 and SS304 show a prolonged  $t_0$  period and limited material degradation, see Figure 7 and Table 3. These alloys exhibit the highest hardness out of all tested materials. Their high resistance to cavitation is due to their strain work hardening and high deformability, which is visualized as the twinning phenomenon (Figure 9e–h). The two-phase ( $\alpha$  and  $\beta'$ ) brass surface damage is more considerable in the  $\alpha$  phase, while the Zn-rich  $\beta'$  phase areas successfully accumulate the cavitation loads, as confirmed by SEM-EDS. Finally, the phase boundaries undergo deformation and open up, which consequently accelerates detachment of the  $\alpha$  phase (Figure 9e,f). While an inverse result was obtained due to the synergetic action of the cavitation-corrosive environment by Abedini et al. [68], they reported that both cavitation corrosion and CE contributed to the degradation of the  $\beta'$  phase. Considering all tested materials, the superior CER was observed for stainless steel. This is attributed to strain hardening of the austenitic microstructure due to deformation. While pitting is observed on its surface (Figure 9g,h) until the end of the test time lasting 30 min, the SS304 sample shows the progression of surface deformation, with no SEM-observable material detachment. This agrees with the findings of our previous research [60] and the observed stainless steel damage mechanism is comparable to that described in the literature [80].

### 3.3. Sliding Wear (SW) of Coatings and Bulk Alloys

A general resistance to wear can be estimated by macroanalysis of worn surface. The set of worn samples presented in Figure 10 indicates narrow wear traces of the composites, comparable to those observed on the SS304 and Cu110 samples. In contrast, uniform and relatively wide wear traces are observed for the AlCu4 and CuZn40 samples. In addition to that, a detailed analysis of the quantitative sliding test results, given in Figure 11 and Table 4, indicates a superior wear resistance of Cu/Al<sub>2</sub>O<sub>3</sub>. Evaluation of the wear factor allows us to state that the copper-based samples exhibit a higher sliding resistance than the aluminium-based samples, Figure 11a. Moreover, both Al/Al<sub>2</sub>O<sub>3</sub> and Cu/Al<sub>2</sub>O<sub>3</sub> exhibit a higher resistance to wear than the low-wear-rate reference stainless steel sample (SS304). Moreover, the friction coefficient of the coatings is higher than those reported for their bulk metal-equivalents, Figure 11b and Table 4. This can be explained by the fact that the wear mechanism of MMCs is affected by their two-phase structure. The Al/Al<sub>2</sub>O<sub>3</sub> sample has the highest average coefficient of friction (COF = 0.764); it is in the range of SD for SS304 (0.697), which, in turn, agrees with the values reported in the literature [81]. The Cu/Al<sub>2</sub>O<sub>3</sub> sample has a COF of 0.555, which is considerably lower

than reported in [38]. From Figure 11b it can be observed that apart from Cu/Al<sub>2</sub>O<sub>3</sub>, the COF of all other samples becomes stable at approximately 100 m, which is attributed to the end of run-in-wear. Therefore, it can be stated that the COF of Cu/Al<sub>2</sub>O<sub>3</sub> could stabilize after a sliding distance exceeding 200 m and its steady-state value could drop below 0.45. This finding is in line with the sliding wear mechanism identified by SEM analysis for the composites and bulk alloys, shown in Figures 12 and 13.

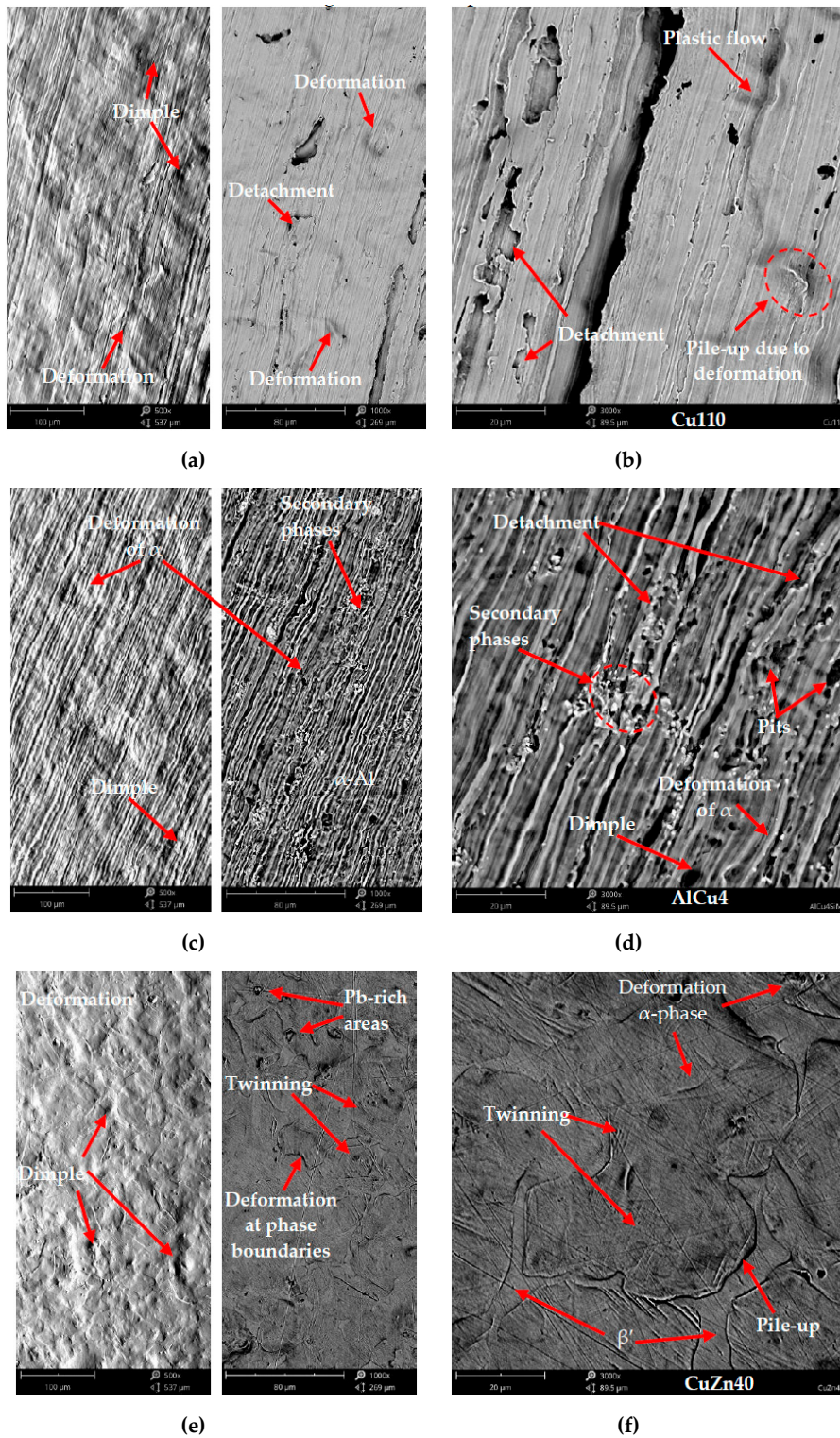
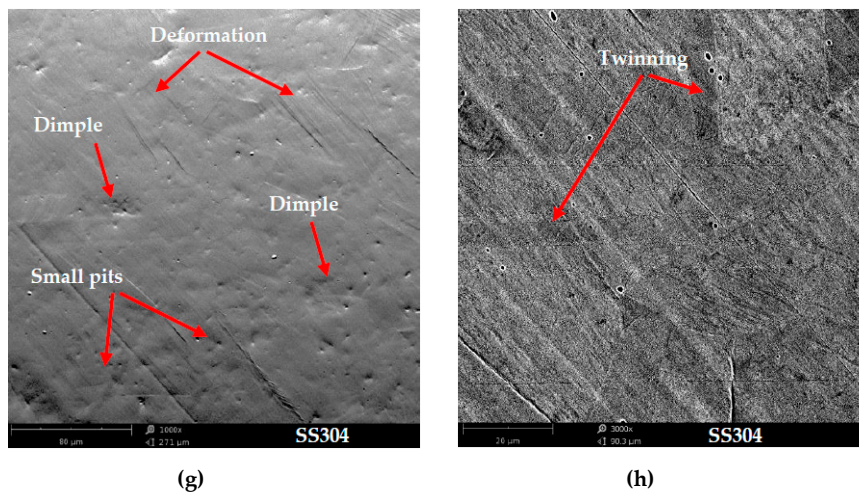
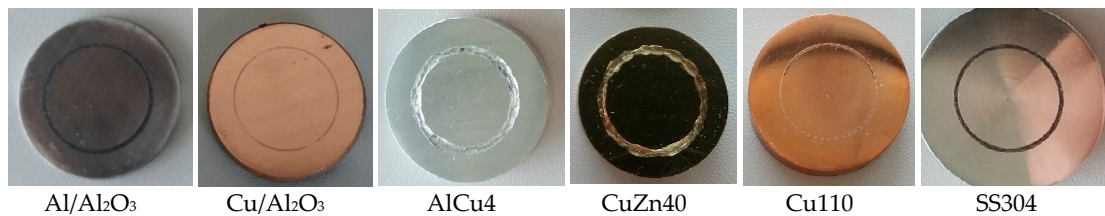


Figure 9. Cont.



**Figure 9.** Eroded surface morphology of reference samples after 4 min of exposition to cavitation: (a,b) AlCu4; (c,d) Cu110; (e,f) CuZn40; (g,h) SS304. SEM, BSE and topo-modes.



**Figure 10.** Macrographs of the wear traces of the cold-sprayed MMC coatings and reference metal alloys.

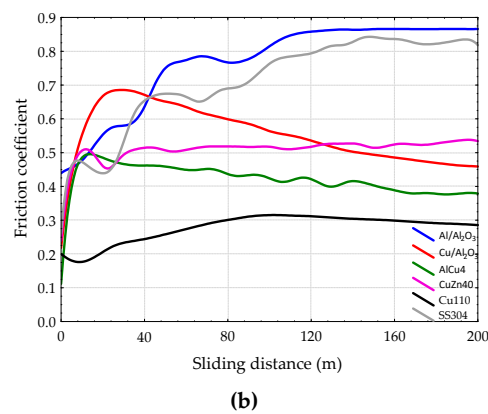
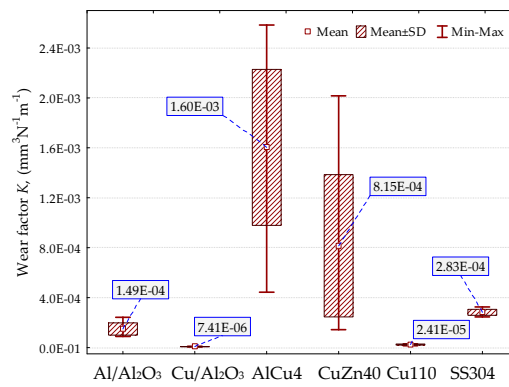


**Figure 11.** Sliding wear results: (a) Wear factor,  $K$ ; (b) a friction coefficient curves.

**Table 4.** The friction coefficient of tested samples.

Specimen	Al/Al <sub>2</sub> O <sub>3</sub>	Cu/Al <sub>2</sub> O <sub>3</sub>	AlCu4	CuZn40	Cu110	SS304
Friction coefficient, mean ± SD	0.764 ± 0.129	0.555 ± 0.081	0.421 ± 0.049	0.512 ± 0.039	0.272 ± 0.042	0.697 ± 0.141

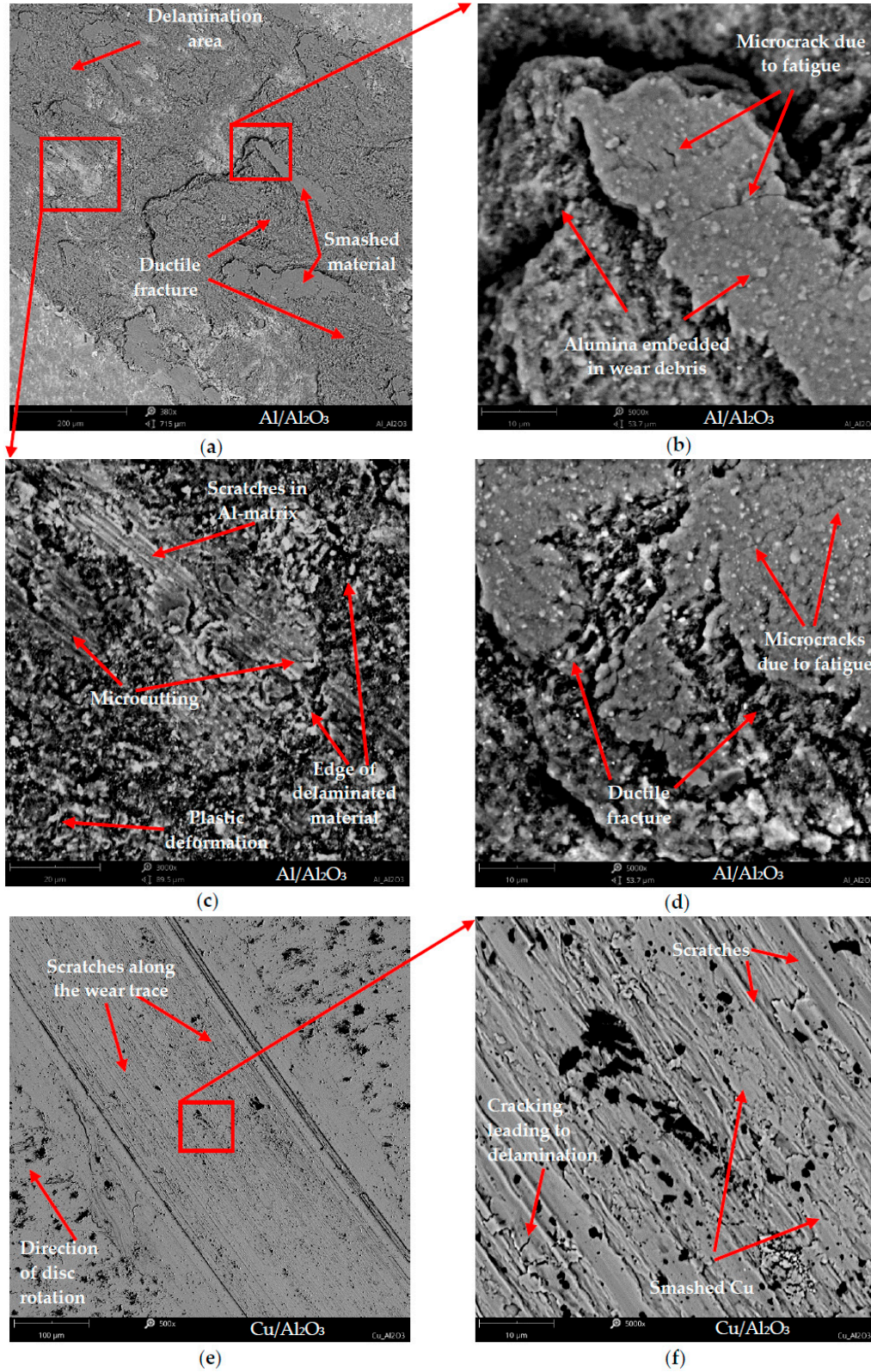


**Figure 12.** Cont.

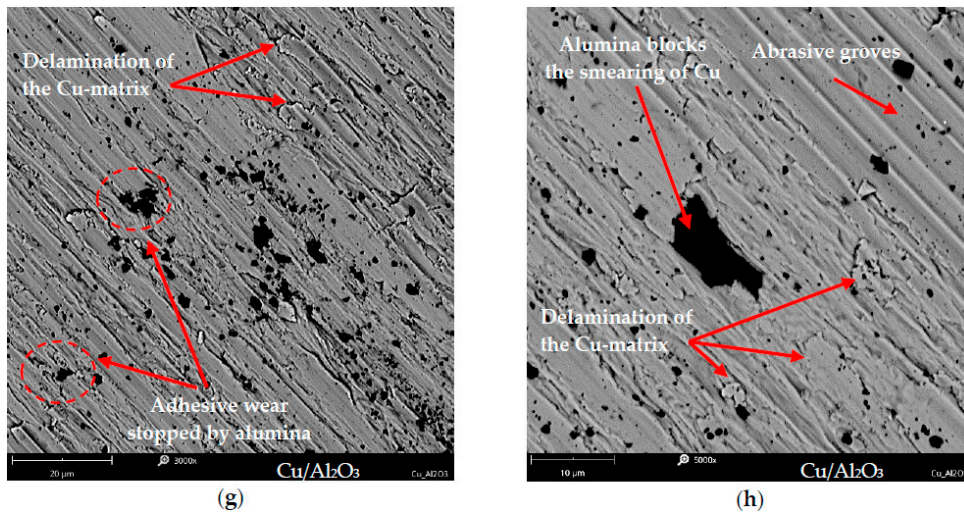


Figure 12. SEM images showing the wear track of cold-sprayed composites: (a–d) Al/Al<sub>2</sub>O<sub>3</sub> and (e–h) Cu/Al<sub>2</sub>O<sub>3</sub>.

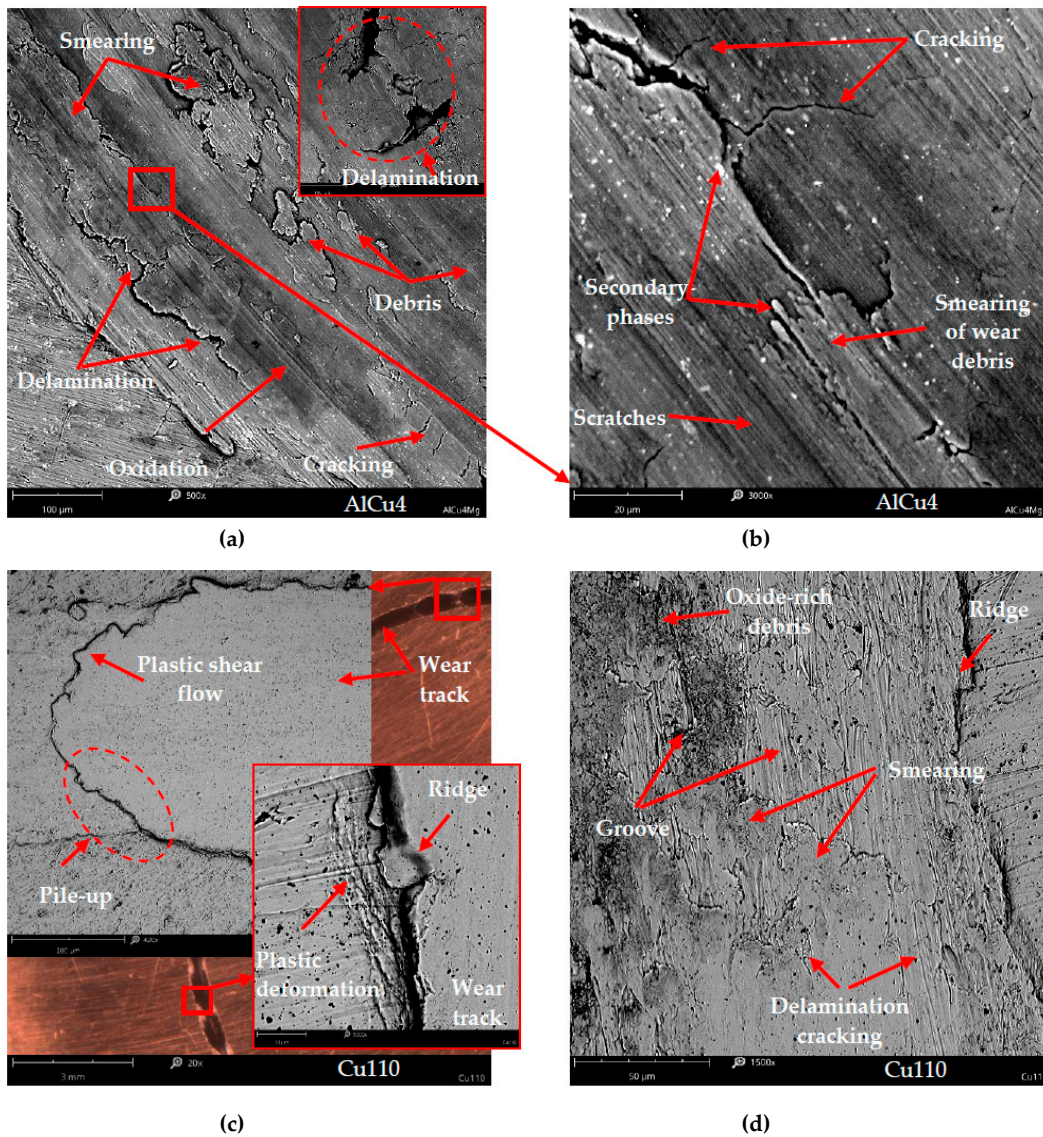
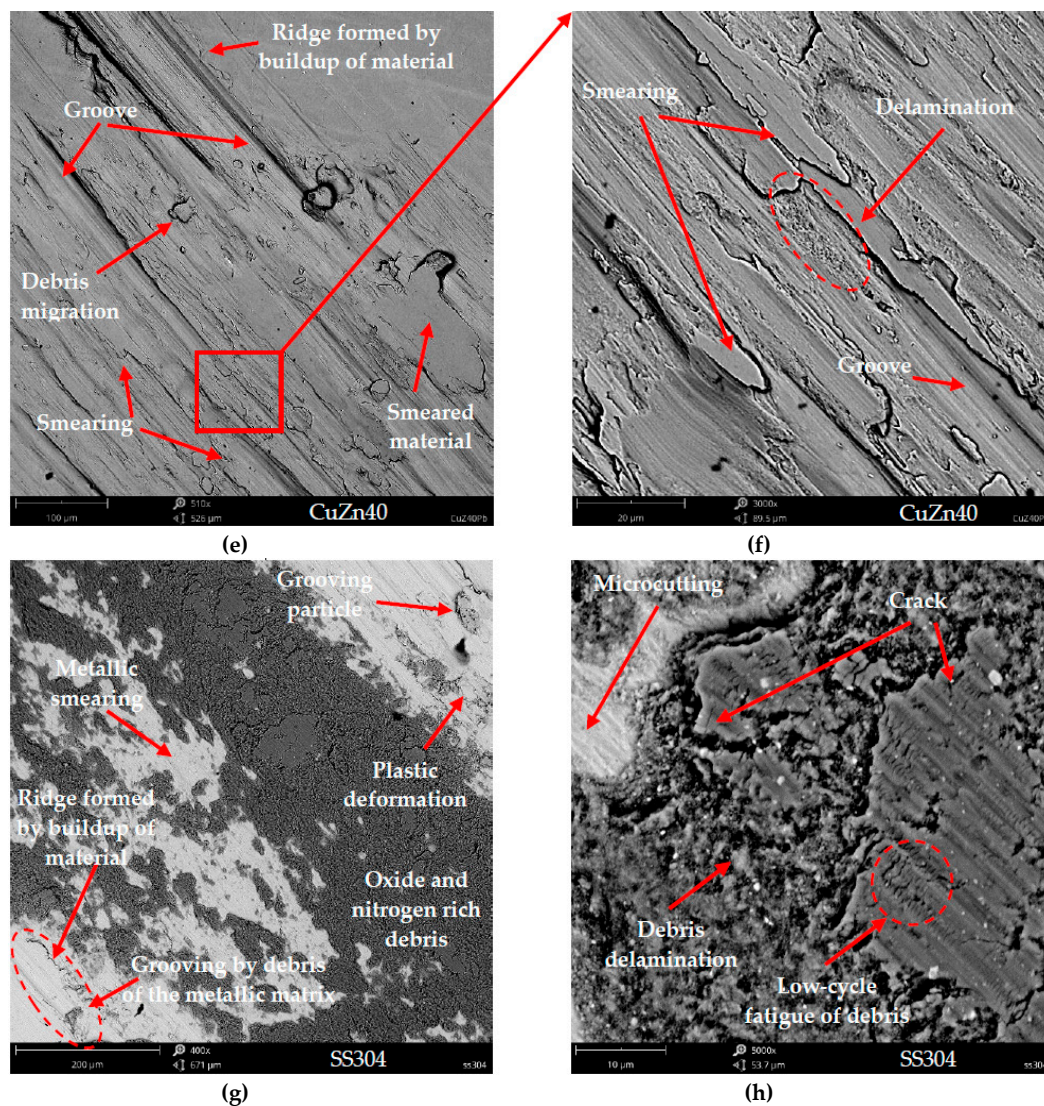


Figure 13. Cont.



**Figure 13.** Comparison of the microimages showing the wear track of bulk alloys: (a,b) AlCu4; (c,d) Cu110; (e,f) CuZn40; (g,h) SS304. SEM-BSE.

To understand their wear mechanisms, the worn surfaces of both Al/Al<sub>2</sub>O<sub>3</sub> and Cu/Al<sub>2</sub>O<sub>3</sub> composites were examined by SEM. Moreover, to determine the effect of the Al- and Cu-matrix reinforcement by alumina, the wear mechanisms of the reference bulk alloys were analysed, too.

The dominant wear mechanism of Al/Al<sub>2</sub>O<sub>3</sub> is adhesive wear combined with micro-abrasive wear, which agrees with the findings reported by other researchers [43,54] for Al-based composites. First, due to the sliding process, clusters of alumina are crushed and wear debris is formed in the wear track. Then, the plastically deformed coating material undergoes delamination, which becomes the wear debris. Agglomerated debris is smashed and the Al-matrix is microcut and low-cycle fatigue is observed, Figure 12a. The delamination of debris-material takes place in a ductile fracture mode. The agglomerates of wear debris are smashed along the wear track and cyclically deformed. This indicates crack formation, which facilitates material detachment, as shown in Figure 12b. Once the debris is transferred through the Al-matrix areas, the hard alumina-contaminants abrade and cut the soft metallic areas, as shown in Figure 12c. This adhesive mechanism relies on systematic delamination, smashing and transfer of the debris material. The low-cycle fatigue enables the formation of cracks, therefore in Figure 12d the cracking of the wear debris is visible. These cracks result from cyclic material deformation and initiate material delamination. Therefore, the alumina particles embedded in the

metallic matrix prevent the composite from severe adhesive wear and worn material pile-up in massive chunks (which can be seen further for aluminium alloy in Figure 13a).

In the case of Cu/Al<sub>2</sub>O<sub>3</sub> the primary wear mechanism is adhesive, which is intensified by abrasive wear. In contrast to the Al/Al<sub>2</sub>O<sub>3</sub> sample, the abrasive wear plays a much more important role in the deterioration of the Cu-based coatings. According to the literature of the subject, the adhesive wear mechanism results in a higher wear rate than the abrasive wear [1]. Thus, the smashing of the Cu matrix dominates, as shown in Figure 12e, and scratches and grooves appear by the alumina-rich wear debris abrasion. The coating material delaminates and is smashed on the wear track, see Figure 12e,f. Besides, the alumina particles block the material transfer (Figure 12g,h); therefore, it is a crucial factor affecting the superior sliding resistance of the Cu/Al<sub>2</sub>O<sub>3</sub> composite. A SEM-EDS wear track and debris analysis shows no significant oxidation of Cu/Al<sub>2</sub>O<sub>3</sub> or increased oxide and nitrogen in the wear debris of Al/Al<sub>2</sub>O<sub>3</sub>. It is well-known that aluminium reacts readily, especially when the temperature in the friction node is increased due to friction.

The sliding wear damage of the reference metal alloys is much more extensive than that of their cold-sprayed composite equivalents, i.e., the sliding wear of AlCu4 is higher than that of Al/Al<sub>2</sub>O<sub>3</sub> and the sliding wear of the Cu110 and CuZn40 samples is higher than that of Cu/Al<sub>2</sub>O<sub>3</sub>. This confirms the quantitative results given in Figure 11. The metallic matrix without the addition of Al<sub>2</sub>O<sub>3</sub> easily degrades, resulting in a high wear factor *K*, see Figure 11a, and a relatively low friction coefficient, Figure 11b. The SEM results confirm that their dominant wear mechanism is adhesive, characterized by a different rate of delaminated-material smearing. Therefore, AlCu4 shows a pure adhesive wear mode, Figure 13a,b, which corresponds to the findings of Alotaibi et al. [82] and Tocci et al. [71]. Large areas of the material are delaminated. This is an effect of surface fatigue due to repeated plastic deformation. Then, the wear debris is smashed along the wear trace. The COF is 0.421, Table 4. Additionally, the soft Al-Cu matrix is scratched by the hard counterball. The SEM-EDS analysis confirms oxidization of the debris. The secondary phases prevent the  $\alpha$ -Al solid solution from smearing, which can be observed in a higher magnification in Figure 13b. However, this effect is negligible to prevent the AlCu4 sample from harsh adhesive damage.

It is reported that the Cu110 sample has a relatively low rate of volume loss. Due to the superior deformability of copper and single-phase microstructure, the adhesive mechanism leads to smearing Cu through the wear track, Figure 13c,d. In effect, limited material delamination occurs. The plastic deformation is visible on the edge of the wear track where some of the worn-material and initial surface pile up (rigid formation). Moreover, plastic shear flow is present in the wear track, see Figure 13c. It can be claimed that the single-phase copper microstructure facilitates sliding, reduces the friction force and therefore results in the lowest friction coefficient from all tested materials, yielding the COF of 0.272 (Table 4). Thus, the delaminated copper and oxides adhere to the counterball, then they smash and form grooves along the sliding direction. In contrast, the two-phase brass (CuZn40) shows a substantial adhesive wear mechanism (Figure 13e,f), characterized by material delamination, severe-smearing, debris migration and deep grooves. Both CuZn40 and AlCu4 have a high wear factor *K*, Figure 11.

The SS304 adhesive wear mechanism is intensified by tribochemical reaction and microcutting (Figure 13g,h), similarly as in [83]. Stainless steel delaminated material undergoes smearing and grooving. The wear products act as an abrasive micro-cutting the exposed stainless steel. The produced debris is oxidized and increases the content of nitrogen, as identified by EDS. This can be explained by the low heat conduction of steel. The temperature increase in the friction node accelerates the chemical reaction between the material and air. Moreover, it should be noted that the wear debris exhibits a low-cycle fatigue mode, Figure 13h, which determines the occurrence of cracking and delamination.

Summing up, the SEM findings show agreement with the quantitative results. The SW damage in the adhesive-abrasive wear of the Al/Al<sub>2</sub>O<sub>3</sub> and Cu/Al<sub>2</sub>O<sub>3</sub> composites is lower than that occurring in the adhesive wear of the bulk metal alloys. Therefore, it is confirmed that the cold-sprayed Al/Al<sub>2</sub>O<sub>3</sub> and Cu/Al<sub>2</sub>O<sub>3</sub> composites enhance the wear resistance of the AISI 304 substrate and Cu/Al<sub>2</sub>O<sub>3</sub> has the superior sliding behaviour out of all tested materials.

#### 4. Conclusions

In this study, an alumina ( $\text{Al}_2\text{O}_3$ ) powder was successfully deposited by the low-pressure cold spray (LPCS) technique with aluminium (Al) and copper (Cu) metallic binders to produce particle-reinforced MMC (metal matrix composite) coatings. The study investigated the cavitation erosion (CE) and sliding wear (SW) behaviours of Al/ $\text{Al}_2\text{O}_3$  and Cu/ $\text{Al}_2\text{O}_3$  composites. Moreover, the CE and SW mechanism of the LPCS coatings were studied too. The wear behaviour of the composites was compared with that of the reference bulk alloys, namely—aluminium alloy (AlCu4), pure copper (Cu110), brass (CuZn40) and stainless steel (SS 304). The results of the study lead to the following conclusions:

1. Surface morphology plays an essential role in cavitation erosion resistance (CER). The as-sprayed LPCS coatings Al/ $\text{Al}_2\text{O}_3$  and Cu/ $\text{Al}_2\text{O}_3$  (with initial roughness and waviness) exhibit a significantly lower CER and almost two-fold higher wear rates than the composites with their surface finished by grinding. Most resistant to cavitation erosion MMC is Cu/ $\text{Al}_2\text{O}_3$  with ground surface finish and presents a cumulative erosion depth of 9.3  $\mu\text{m}$ , while the highest erosion depth of 53.4  $\mu\text{m}$  was obtained for the as-sprayed Al/ $\text{Al}_2\text{O}_3$ . In contrast to the composites, bulk alloys have a prolonged incubation period of CE and lower wear rates. The CER characterized by the maximum erosion rate increases according to the following pattern: Al/ $\text{Al}_2\text{O}_3$  < Cu/ $\text{Al}_2\text{O}_3$  < Cu110 < AlCu4 < CuZn40 < SS 304, which corresponds to the values of 33.4  $\text{mm}^3/\text{h}$ ; 14.8  $\text{mm}^3/\text{h}$ ; 10.9  $\text{mm}^3/\text{h}$ ; 4.6  $\text{mm}^3/\text{h}$ ; 0.7  $\text{mm}^3/\text{h}$ ; and zero for SS 304, respectively. Therefore, the CER of the bulk alloys exceeds that obtained for the LPCS composites.
2. The addition of the alumina ( $\text{Al}_2\text{O}_3$ ) reinforcing particles effectively increases the SW resistance of metallic materials by lowering the material loss and the wear factor ( $K$ ) of composites. Generally, the LPCS Cu/ $\text{Al}_2\text{O}_3$  coating exhibits a superior SW resistance ( $K = 7.41 \times 10^{-7} \text{mm}^3 \cdot \text{N}^{-1} \cdot \text{m}^{-1}$ ) than the aluminium alloy (AlCu4;  $K = 1.6 \times 10^{-3} \text{mm}^3 \cdot \text{N}^{-1} \cdot \text{m}^{-1}$ ), brass (CuZn40;  $K = 8.15 \times 10^{-4} \text{mm}^3 \cdot \text{N}^{-1} \cdot \text{m}^{-1}$ ), stainless steel (SS 304;  $K = 2.84 \times 10^{-4} \text{mm}^3 \cdot \text{N}^{-1} \cdot \text{m}^{-1}$ ), Al/ $\text{Al}_2\text{O}_3$  coating ( $K = 1.49 \times 10^{-4} \text{mm}^3 \cdot \text{N}^{-1} \cdot \text{m}^{-1}$ ) and pure copper (Cu110;  $K = 2.14 \times 10^{-6} \text{mm}^3 \cdot \text{N}^{-1} \cdot \text{m}^{-1}$ ). On the other hand, the presence of ceramic particles in the microstructure of Al/ $\text{Al}_2\text{O}_3$  and Cu/ $\text{Al}_2\text{O}_3$  composites results a relatively high friction coefficient of 0.764 and 0.555, respectively, while the coefficients of friction of the bulk alloys Cu110, AlCu4, CuZn40 and SS 304 is 0.272; 0.421; 0.512 and 0.697, respectively.
3. The microstructure of the material plays a crucial role in cavitation wear resistance. In contrast to the bulk alloys, the two-phase, metallic-ceramic composite microstructure of the MMC composite results in severe erosion due to cavitation. The wear mechanisms of the LPCS composites start at the structural discontinuities and non-uniformities as well as ceramic-metallic matrix interfaces, pores and rough surface dimples. Additionally, the Al/ $\text{Al}_2\text{O}_3$  damage mechanism relies on the chunk material detachment, while the damage of Cu/ $\text{Al}_2\text{O}_3$  is initiated by alumina removal and further proceeds in a layer-like removal of the Cu-metallic material. In turn, the cavitation erosion damage of metal alloys relies on the removal of fatigue-induced plastic deformation of the material started at surface non-uniformities or at microstructural phase boundaries.
4. The sliding wear mechanism of the LPCS composites is characterized by an adhesive-abrasive mode. Additionally, Al/ $\text{Al}_2\text{O}_3$  wear behaviour was dominated by an adhesive wear-debris transfer, once in Cu/ $\text{Al}_2\text{O}_3$  the abrasion was much produced and adhesive damage was controlled by the reinforcing alumina particles. In contrast to the bulk alloys, the addition of  $\text{Al}_2\text{O}_3$  successfully reduces the wear factor ( $K$ ). In turn, considerable wear due to the adhesive wear mechanism was observed for all metallic reference samples, especially for AlCu4 and CuZn40. The Cu110 sample showed a light adhesive wear mode supported by oxidation. Moreover, the adhesive failure mechanism of the SS 304 samples was intensified by a tribochemical reaction, thus oxide and nitrogen-enriched debris were identified in the wear track.
5. Summing up, the cold spray-deposited Al/ $\text{Al}_2\text{O}_3$  and Cu/ $\text{Al}_2\text{O}_3$  composites can be successfully applied as coatings for increasing SW resistance, thus enhancing the wear resistance of the AISI 304

substrate. Moreover, the Cu/Al<sub>2</sub>O<sub>3</sub> composite has a superior cavitation and SW resistance than the Al/Al<sub>2</sub>O<sub>3</sub> coating. However, these coatings have a lower cavitation erosion resistance than all reference materials, namely—aluminium alloy (AlCu4), pure copper (Cu110), brass (CuZn40) and stainless steel (SS 304).

**Author Contributions:** Conceptualization, M.S.; methodology, M.S., L.Ł., M.W. (Mariusz Walczak) and M.W. (Marcin Winnicki); software, M.S.; validation, M.S., L.Ł., M.W. (Mariusz Walczak) and M.W. (Marcin Winnicki); formal analysis, M.S. and L.Ł.; investigation, M.S., L.Ł. and M.W. (Mariusz Walczak); resources, M.S., L.Ł., M.W. (Mariusz Walczak) and M.W. (Marcin Winnicki); data curation, M.S.; writing—original draft preparation, M.S.; writing—review and editing, M.S. and L.Ł.; visualization, M.S., M.W. (Mariusz Walczak) and M.W. (Marcin Winnicki); supervision, M.S.; project administration, M.S.; funding acquisition, M.S. and L.Ł. All authors have read and agreed to the published version of the manuscript.

**Funding:** The research was financed in the framework of the project Lublin University of Technology—Regional Excellence Initiative, funded by the Polish Ministry of Science and Higher Education (contract No. 030/RID/2018/19).

**Conflicts of Interest:** The authors declare no conflict of interest.

## References

1. Wen, S.; Huang, P. *Principles of Tribology*, 1st ed.; Wiley: Hoboken, NJ, USA, 2012; ISBN 978-1-118-06289-0.
2. Tomków, J.; Czupryński, A.; Fydrych, D. The abrasive wear resistance of coatings manufactured on high-strength low-alloy (HSLA) offshore steel in wet welding conditions. *Coatings* **2020**, *10*, 219. [[CrossRef](#)]
3. Al-Hamed, A.; Al-Fadhli, H.Y.; Al-Mutairi, S.; Yilbas, B.S.; Hashmi, M.S.J.; Stokes, J. Investigation of HVOF thermal sprayed nanostructured WC-12Co mixed with Inconel-625 coatings for oil/gas applications. In *Surface Effects and Contact Mechanics XI*; WIT Transactions on Engineering Sciences; WIT Press: Southampton, UK, 2013; Volume 78, pp. 215–225.
4. Szala, M.; Szafran, M.; Macek, W.; Marchenko, S.; Hejwowski, T. Abrasion resistance of S235, S355, C45, AISI 304 and Hardox 500 steels with usage of garnet, corundum and carborundum abrasives. *Adv. Sci. Technol. Res. J.* **2019**, *13*, 151–161. [[CrossRef](#)]
5. Krebs, S.; Gaertner, F.; Klassen, T. Cold spraying of Cu-Al-Bronze for cavitation protection in marine environments. *Mater. Werkst.* **2014**, *45*, 708–716. [[CrossRef](#)]
6. Hou, B.-R.; Zhang, J.; Duan, J.-Z.; Li, Y.; Zhang, J.-L. Corrosion of thermally sprayed zinc and aluminium coatings in simulated splash and tidal zone conditions. *Corros. Eng. Sci. Technol.* **2003**, *38*, 157–160. [[CrossRef](#)]
7. Verna, E.; Biagi, R.; Kazasidis, M.; Galetto, M.; Bemporad, E.; Lupoi, R. Modeling of erosion response of cold-sprayed In718-Ni composite coating using full factorial design. *Coatings* **2020**, *10*, 335. [[CrossRef](#)]
8. Zakrzewska, D.E.; Krella, A.K. Cavitation erosion resistance influence of material properties. *Adv. Mater. Sci.* **2019**, *19*, 18–34. [[CrossRef](#)]
9. Du, J.; Zhang, J.; Zhang, C. Effect of heat treatment on the cavitation erosion performance of WC-12Co coatings. *Coatings* **2019**, *9*, 690. [[CrossRef](#)]
10. Szymański, K.; Hernas, A.; Moskal, G.; Myalska, H. Thermally sprayed coatings resistant to erosion and corrosion for power plant boilers—A review. *Surf. Coat. Technol.* **2015**, *268*, 153–164. [[CrossRef](#)]
11. Zoei, M.S.; Sadeghi, M.H.; Salehi, M. Effect of grinding parameters on the wear resistance and residual stress of HVOF-deposited WC-10Co-4Cr coating. *Surf. Coat. Technol.* **2016**, *307*, 886–891. [[CrossRef](#)]
12. Goyal, D.K.; Singh, H.; Kumar, H.; Sahni, V. Slurry erosive wear evaluation of HVOF-spray Cr<sub>2</sub>O<sub>3</sub> coating on some turbine steels. *J. Therm. Spray Technol.* **2012**, *21*, 838–851. [[CrossRef](#)]
13. Singh, J.; Kumar, S.; Mohapatra, S.K. An erosion and corrosion study on thermally sprayed WC-Co-Cr powder synergized with Mo<sub>2</sub>C/Y<sub>2</sub>O<sub>3</sub>/ZrO<sub>2</sub> feedstock powders. *Wear* **2019**, *438–439*, 1027512. [[CrossRef](#)]
14. Lavigne, S.; Pougoum, F.; Savoie, S.; Martinu, L.; Klemberg-Sapieha, J.E.; Schulz, R. Cavitation erosion behavior of HVOF CaviTec coatings. *Wear* **2017**, *386–387*, 90–98. [[CrossRef](#)]
15. Koga, G.Y.; Wolf, W.; Schulz, R.; Savoie, S.; Bolfarini, C.; Kiminami, C.S.; Botta, W.J. Corrosion and wear properties of FeCrMnCoSi HVOF coatings. *Surf. Coat. Technol.* **2019**, *357*, 993–1003. [[CrossRef](#)]
16. Yang, K.; Li, J.; Wang, Q.; Li, Z.; Jiang, Y.; Bao, Y. Effect of laser remelting on microstructure and wear resistance of plasma sprayed Al<sub>2</sub>O<sub>3</sub>-40% TiO<sub>2</sub> coating. *Wear* **2019**, *426–427*, 314–318. [[CrossRef](#)]
17. Yang, K.; Rong, J.; Feng, J.; Zhuang, Y.; Zhao, H.; Wang, L.; Ni, J.; Tao, S.; Shao, F.; Ding, C. Excellent wear resistance of plasma-sprayed amorphous Al<sub>2</sub>O<sub>3</sub>-Y<sub>3</sub>Al<sub>5</sub>O<sub>12</sub> ceramic coating. *Surf. Coat. Technol.* **2017**, *326*, 96–102. [[CrossRef](#)]

18. Mao, Z.; Wang, J.; Sun, B.; Bordia, R.K. Wear resistance of reactive plasma sprayed and laser remelted TiB<sub>2</sub>-TiC<sub>0.3</sub>N<sub>0.7</sub> based composite coatings against medium carbon steel. *Appl. Surf. Sci.* **2011**, *257*, 2610–2616. [[CrossRef](#)]
19. Chen, L.-Y.; Xu, T.; Lu, S.; Wang, Z.-X.; Chen, S.; Zhang, L.-C. Improved hardness and wear resistance of plasma sprayed nanostructured NiCrBSi coating via short-time heat treatment. *Surf. Coat. Technol.* **2018**, *350*, 436–444. [[CrossRef](#)]
20. Wen, Z.H.; Bai, Y.; Yang, J.F.; Huang, J.; Zhang, L. Effect of vacuum remelting on microstructure and wear resistance of NiCrMoY coatings deposited by supersonic atmospheric plasma spraying. *Surf. Coat. Technol.* **2015**, *281*, 62–67. [[CrossRef](#)]
21. Wang, Y.; Liu, J.; Kang, N.; Darut, G.; Poirier, T.; Stella, J.; Liao, H.; Planche, M.-P. Cavitation erosion of plasma-sprayed CoMoCrSi coatings. *Tribol. Int.* **2016**, *102*, 429–435. [[CrossRef](#)]
22. Szala, M.; Dudek, A.; Maruszczak, A.; Walczak, M.; Chmiel, J.; Kowal, M. Effect of atmospheric plasma sprayed TiO<sub>2</sub>-10% NiAl cermet coating thickness on cavitation erosion, sliding and abrasive wear resistance. *Acta Phys. Pol. A* **2019**, *136*, 335–341. [[CrossRef](#)]
23. Molins, R.; Normand, B.; Rannou, G.; Hannover, B.; Liao, H. Interlamellar boundary characterization in Ni-based alloy thermally sprayed coating. *Mater. Sci. Eng. A* **2003**, *351*, 325–333. [[CrossRef](#)]
24. Pardo, A.; Casajús, P.; Mohedano, M.; Coy, A.E.; Viejo, F.; Torres, B.; Matykina, E. Corrosion protection of Mg/Al alloys by thermal sprayed aluminium coatings. *Appl. Surf. Sci.* **2009**, *255*, 6968–6977. [[CrossRef](#)]
25. Fauchais, P.L.; Heberlein, J.V.R.; Boulos, M.I. Fundamentals of combustion and thermal plasma. In *Thermal Spray Fundamentals*; Springer: Boston, MA, USA, 2014; pp. 73–111, ISBN 978-0-387-28319-7.
26. Winnicki, M.; Piwowarczyk, T.; Małachowska, A. General description of cold sprayed coatings formation and of their properties. *Bull. Pol. Acad. Sci. Tech. Sci.* **2018**, *66*, 301–310.
27. Sun, W.; Tan, A.W.-Y.; Wu, K.; Yin, S.; Yang, X.; Marinescu, I.; Liu, E. Post-process treatments on supersonic cold sprayed coatings: A review. *Coatings* **2020**, *10*, 123. [[CrossRef](#)]
28. Koivuluoto, H.; Larjo, J.; Marini, D.; Pulci, G.; Marra, F. Cold-sprayed Al6061 coatings: Online spray monitoring and influence of process parameters on coating properties. *Coatings* **2020**, *10*, 348. [[CrossRef](#)]
29. Meng, F.; Yue, S.; Song, J. Quantitative prediction of critical velocity and deposition efficiency in cold-spray: A finite-element study. *Scr. Mater.* **2015**, *107*, 83–87. [[CrossRef](#)]
30. Kumar, S.; Vidyasagar, V.; Jyothirmayi, A.; Joshi, S.V. Effect of heat treatment on mechanical properties and corrosion performance of cold-sprayed tantalum coatings. *J. Therm. Spray Technol.* **2016**, *25*, 745–756. [[CrossRef](#)]
31. Zhang, Y.; Shockley, J.M.; Vo, P.; Chromik, R.R. Tribological behavior of a cold-sprayed Cu–MoS<sub>2</sub> composite coating during dry sliding wear. *Tribol. Lett.* **2016**, *62*. [[CrossRef](#)]
32. Meyer, M.C.; Yin, S.; McDonnell, K.A.; Stier, O.; Lupoi, R. Feed rate effect on particulate acceleration in Cold Spray under low stagnation pressure conditions. *Surf. Coat. Technol.* **2016**, *304*, 237–245. [[CrossRef](#)]
33. King, P.C.; Zahiri, S.; Jahedi, M.; Friend, J. Aluminium coating of lead zirconate titanate—A study of cold spray variables. *Surf. Coat. Technol.* **2010**, *205*, 2016–2022. [[CrossRef](#)]
34. Winnicki, M.; Baszczuk, A.; Jasiorski, M.; Małachowska, A. Corrosion resistance of copper coatings deposited by cold spraying. *J. Therm. Spray Technol.* **2017**, *26*, 1935–1946. [[CrossRef](#)]
35. Lee, Y.T.R.; Ashrafizadeh, H.; Fisher, G.; McDonald, A. Effect of type of reinforcing particles on the deposition efficiency and wear resistance of low-pressure cold-sprayed metal matrix composite coatings. *Surf. Coat. Technol.* **2017**, *324*, 190–200. [[CrossRef](#)]
36. Chen, W.; Yu, Y.; Cheng, J.; Wang, S.; Zhu, S.; Liu, W.; Yang, J. Microstructure, mechanical properties and dry sliding wear behavior of Cu-Al<sub>2</sub>O<sub>3</sub>-graphite solid-lubricating coatings deposited by low-pressure cold spraying. *J. Therm. Spray Technol.* **2018**, *27*, 1652–1663. [[CrossRef](#)]
37. Zhang, Y.; Choudhuri, D.; Scharf, T.W.; Descartes, S.; Chromik, R.R. Tribologically induced nanolaminate in a cold-sprayed WC-reinforced Cu matrix composite: A key to high wear resistance. *Mater. Des.* **2019**, *182*, 108009. [[CrossRef](#)]
38. Zhang, L.; Yang, S.; Lv, X.; Jie, X. Wear and corrosion resistance of cold-sprayed Cu-based composite coatings on magnesium substrate. *J. Therm. Spray Technol.* **2019**, *28*, 1212–1224. [[CrossRef](#)]
39. Jenkins, R.; Yin, S.; Aldwell, B.; Meyer, M.; Lupoi, R. New insights into the in-process densification mechanism of cold spray Al coatings: Low deposition efficiency induced densification. *J. Mater. Sci. Technol.* **2019**, *35*, 427–431. [[CrossRef](#)]

40. Wang, Y.; Normand, B.; Suo, X.; Planche, M.-P.; Liao, H.; Tang, J. Cold-sprayed AZ91D coating and SiC/AZ91D composite coatings. *Coatings* **2018**, *8*, 122. [[CrossRef](#)]
41. Wang, Y.; Normand, B.; Liao, H.; Zhao, G.; Mary, N.; Tang, J. SiCp/Al5056 composite coatings applied to a magnesium substrate by cold gas dynamic spray method for corrosion protection. *Coatings* **2020**, *10*, 325. [[CrossRef](#)]
42. Winnicki, M.; Małachowska, A.; Piwowarczyk, T.; Rutkowska-Gorczyca, M.; Ambroziak, A. The bond strength of Al + Al<sub>2</sub>O<sub>3</sub> cermet coatings deposited by low-pressure cold spraying. *Arch. Civ. Mech. Eng.* **2016**, *16*, 743–752. [[CrossRef](#)]
43. Cong, D.; Li, Z.; He, Q.; Chen, H.; Zhao, Z.; Zhang, L.; Wu, H. Wear behavior of corroded Al-Al<sub>2</sub>O<sub>3</sub> composite coatings prepared by cold spray. *Surf. Coat. Technol.* **2017**, *326*, 247–254. [[CrossRef](#)]
44. Chen, X.; Li, C.; Xu, S.; Hu, Y.; Ji, G.; Wang, H. Microstructure and microhardness of Ni/Al-TiB<sub>2</sub> composite coatings prepared by cold spraying combined with postannealing treatment. *Coatings* **2019**, *9*, 565. [[CrossRef](#)]
45. Hu, H.X.; Jiang, S.L.; Tao, Y.S.; Xiong, T.Y.; Zheng, Y.G. Cavitation erosion and jet impingement erosion mechanism of cold sprayed Ni-Al<sub>2</sub>O<sub>3</sub> coating. *Nucl. Eng. Des.* **2011**, *241*, 4929–4937. [[CrossRef](#)]
46. Lu, X.; Wang, S.; Xiong, T.; Wen, D.; Wang, G.; Du, H. Anticorrosion properties of Zn-Al composite coating prepared by cold spraying. *Coatings* **2019**, *9*, 210. [[CrossRef](#)]
47. Wang, K.; Wang, S.; Xiong, T.; Wen, D.; Wang, G.; Liu, W.; Du, H. Protective performance of Zn-Al-Mg-TiO<sub>2</sub> coating prepared by cold spraying on marine steel equipment. *Coatings* **2019**, *9*, 339. [[CrossRef](#)]
48. Winnicki, M.; Małachowska, A.; Rutkowska-Gorczyca, M.; Sokołowski, P.; Ambroziak, A.; Pawłowski, L. Characterization of cermet coatings deposited by low-pressure cold spraying. *Surf. Coat. Technol.* **2015**, *268*, 108–114. [[CrossRef](#)]
49. Sova, A.; Papyrin, A.; Smurov, I. Influence of ceramic powder size on process of cermet coating formation by cold spray. *J. Therm. Spray Technol.* **2009**, *18*, 633. [[CrossRef](#)]
50. Kumari, K.; Anand, K.; Bellacci, M.; Giannozzi, M. Effect of microstructure on abrasive wear behavior of thermally sprayed WC-10Co-4Cr coatings. *Wear* **2010**, *268*, 1309–1319. [[CrossRef](#)]
51. Ralph, B.; Yuen, H.C.; Lee, W.B. The processing of metal matrix composites—An overview. *J. Mater. Process. Technol.* **1997**, *63*, 339–353. [[CrossRef](#)]
52. Irissou, E.; Legoux, J.-G.; Arsenault, B.; Moreau, C. Investigation of Al-Al<sub>2</sub>O<sub>3</sub> cold spray coating formation and properties. *J. Therm. Spray Technol.* **2007**, *16*, 661–668. [[CrossRef](#)]
53. Meydanoglu, O.; Jodoin, B.; Kayali, E.S. Microstructure, mechanical properties and corrosion performance of 7075 Al matrix ceramic particle reinforced composite coatings produced by the cold gas dynamic spraying process. *Surf. Coat. Technol.* **2013**, *235*, 108–116. [[CrossRef](#)]
54. Pitchuka, S.B.; Boesl, B.; Zhang, C.; Lahiri, D.; Nieto, A.; Sundararajan, G.; Agarwal, A. Dry sliding wear behavior of cold sprayed aluminum amorphous/nanocrystalline alloy coatings. *Surf. Coat. Technol.* **2014**, *238*, 118–125. [[CrossRef](#)]
55. Kazasidis, M.; Yin, S.; Cassidy, J.; Volkov-Husović, T.; Vlahović, M.; Martinović, S.; Kyriakopoulou, E.; Lupoi, R. Microstructure and cavitation erosion performance of nickel-Inconel 718 composite coatings produced with cold spray. *Surf. Coat. Technol.* **2020**, *382*, 125195. [[CrossRef](#)]
56. Matikainen, V.; Niemi, K.; Koivuluoto, H.; Vuoristo, P. Abrasion, erosion and cavitation erosion wear properties of thermally sprayed alumina based coatings. *Coatings* **2014**, *4*, 18–36. [[CrossRef](#)]
57. Matikainen, V.; Koivuluoto, H.; Vuoristo, P. A study of Cr<sub>3</sub>C<sub>2</sub>-based HVOF- and HVOF-sprayed coatings: Abrasion, dry particle erosion and cavitation erosion resistance. *Wear* **2020**, *446–447*, 203188. [[CrossRef](#)]
58. Szala, M.; Walczak, M.; Pasierbiewicz, K.; Kamiński, M. Cavitation erosion and sliding wear mechanisms of AlTiN and TiAlN films deposited on stainless steel substrate. *Coatings* **2019**, *9*, 340. [[CrossRef](#)]
59. Michalak, M.; Łatka, L.; Sokołowski, P.; Niemiec, A.; Ambroziak, A. The microstructure and selected mechanical properties of Al<sub>2</sub>O<sub>3</sub> + 13 wt.% TiO<sub>2</sub> plasma sprayed coatings. *Coatings* **2020**, *10*, 173. [[CrossRef](#)]
60. Łatka, L.; Szala, M.; Michalak, M.; Pałka, T. Impact of atmospheric plasma spray parameters on cavitation erosion resistance of Al<sub>2</sub>O<sub>3</sub>-13%TiO<sub>2</sub> coatings. *Acta Phys. Pol. A* **2019**, *136*, 342–347. [[CrossRef](#)]
61. ASTM International. *ASTM G32-10: Standard Test. Method for Cavitation Erosion Using Vibratory Apparatus*; ASTM International: West Conshohocken, PA, USA, 2010.
62. ASTM International. *ASTM G99-95a: Standard Test. Method for Wear Testing with a Pin-on-Disk Apparatus*; ASTM International: West Conshohocken, PA, USA, 2000.
63. Walczak, M.; Pieniak, D.; Niewczas, A.M. Effect of recasting on the useful properties CoCrMoW alloy. *Eksploat. Niezawodn. Maint. Reliab.* **2014**, *16*, 330–336.

64. Davis, J.R. *Handbook of Thermal Spray Technology*; ASM International: Cleveland, OH, USA, 2004; ISBN 978-0-87170-795-6.
65. Yu, M.; Li, W. Metal matrix composite coatings by cold spray. In *Cold-Spray Coatings: Recent Trends and Future perspectives*; Cavaliere, P., Ed.; Springer International Publishing: Cham, Switzerland, 2018; pp. 297–318, ISBN 978-3-319-67183-3.
66. Kubatík, T.F.; Pala, Z.; Neufuss, K.; Vilémová, M.; Mušálek, R.; Stouřil, J.; Slepíčka, P.; Chráška, T. Metallurgical bond between magnesium AZ91 alloy and aluminium plasma sprayed coatings. *Surf. Coat. Technol.* **2015**, *282*, 163–170. [[CrossRef](#)]
67. Torres, B.; Taltavull, C.; López, A.J.; Campo, M.; Rams, J. Al/SiCp and Al11Si/SiCp coatings on AZ91 magnesium alloy by HVOF. *Surf. Coat. Technol.* **2015**, *261*, 130–140. [[CrossRef](#)]
68. Abedini, M.; Reuter, F.; Hanke, S. Corrosion and material alterations of a CuZn38Pb3 brass under acoustic cavitation. *Ultrason. Sonochem.* **2019**, *58*, 104628. [[CrossRef](#)] [[PubMed](#)]
69. Jourani, A.; Bouvier, S. Friction and wear mechanisms of 316L stainless steel in dry sliding contact: Effect of abrasive particle size. *Tribol. Trans.* **2015**, *58*, 131–139. [[CrossRef](#)]
70. Dybowski, B.; Szala, M.; Kielbus, A.; Hejwowski, T.J. The mechanisms of cavitation erosion of the Elektron21 magnesium alloy. In *Solid State Phenomena*; Trans Tech Publications Ltd.: Zurich, Switzerland, 2015; Volume 229, pp. 99–104. [[CrossRef](#)]
71. Tocci, M.; Pola, A.; Girelli, L.; Lollo, F.; Montesano, L.; Gelfi, M. Wear and cavitation erosion resistance of an AlMgSc alloy produced by DMLS. *Metals* **2019**, *9*, 308. [[CrossRef](#)]
72. Steller, J. International Cavitation Erosion Test and quantitative assessment of material resistance to cavitation. *Wear* **1999**, *233–235*, 51–64. [[CrossRef](#)]
73. Szala, M.; Hejwowski, T. Cavitation erosion resistance and wear mechanism model of flame-sprayed Al<sub>2</sub>O<sub>3</sub>-40%TiO<sub>2</sub>/NiMoAl cermet coatings. *Coatings* **2018**, *8*, 254. [[CrossRef](#)]
74. Szala, M. Application of computer image analysis software for determining incubation period of cavitation erosion—Preliminary results. In Proceedings of the ITM Web of Conferences, Lublin, Poland, 23–25 November 2017; Volume 15, p. 06003. [[CrossRef](#)]
75. Hong Yu, Y.Z.; Hong Yu, Y.Z. Cavitation erosion corrosion behaviour of manganese-nickel-aluminum bronze in comparison with manganese-brass. *J. Mater. Sci. Technol.* **2009**, *25*, 758–766.
76. Richman, R.H.; McNaughton, W.P. Correlation of cavitation erosion behavior with mechanical properties of metals. *Wear* **1990**, *140*, 63–82. [[CrossRef](#)]
77. Richman, R.H.; McNaughton, W.P. A metallurgical approach to improved cavitation-erosion resistance. *J. Mater. Eng. Perform.* **1997**, *6*, 633–641. [[CrossRef](#)]
78. Krella, A.K.; Zakrzewska, D.E.; Marchewicz, A. The resistance of S235JR steel to cavitation erosion. *Wear* **2020**, *452–453*, 203295. [[CrossRef](#)]
79. Dybowski, B.; Szala, M.; Hejwowski, T.J.; Kielbus, A. Microstructural phenomena occurring during early stages of cavitation erosion of Al-Si aluminium casting alloys. In *Solid State Phenomena*; Trans Tech Publications Ltd.: Zurich, Switzerland, 2015; Volume 227, pp. 255–258. [[CrossRef](#)]
80. Bregliozzi, G.; Schino, A.D.; Ahmed, S.I.-U.; Kenny, J.M.; Haefke, H. Cavitation wear behaviour of austenitic stainless steels with different grain sizes. *Wear* **2005**, *258*, 503–510. [[CrossRef](#)]
81. Spencer, K.; Fabijanic, D.M.; Zhang, M.-X. The use of Al–Al<sub>2</sub>O<sub>3</sub> cold spray coatings to improve the surface properties of magnesium alloys. *Surf. Coat. Technol.* **2009**, *204*, 336–344. [[CrossRef](#)]
82. Alotaibi, J.; Yousif, B.; Yusaf, T. Wear behaviour and mechanism of different metals sliding against stainless steel counterface. *Proc. Inst. Mech. Eng. Part J J. Eng. Tribol.* **2014**, *228*, 692–704. [[CrossRef](#)]
83. Straffellini, G.; Molinari, A.; Trabucco, D. Sliding wear of austenitic and austenitic-ferritic stainless steels. *Metall. Mater. Trans. A* **2002**, *33*, 613–624. [[CrossRef](#)]

